High-speed nanoindentation mapping of organic matter-rich rocks: A critical evaluation by correlative imaging and machine learning data analysis

S. Vranjes-Wessely [a,b,*], D. Misch [a], D. Kiener [b], M.J. Cordill [c], N. Frese [d], A. Beyer [d], B. Horsfield [e], C. Wang [f], R.F. Sachsenhofer [a]

[a] *Department of Applied Geosciences and Geophysics, Montanuniversitaet Leoben, A-8700 Leoben, Austria*
[b] *Department of Materials Science, Montanuniversitaet Leoben, A-8700 Leoben, Austria*
[c] *Erich Schmid Institute of Materials Science, Austrian Academy of Sciences, A-8700 Leoben, Austria*
[d] *Faculty of Physics, Bielefeld University, D-33615 Bielefeld, Germany*
[e] *GEOS4 GmbH, D-14552 Michendorf, Germany*
[f] *State Key Laboratory of Biogeology and Environmental Geology, China University of Geosciences, Beijing, China*

ARTICLE INFO

ABSTRACT

Nanoindentation is a valuable tool, which enables insights into the material properties of natural, highly inhomogeneous composite materials such as shales and organic matter-rich rocks. However, the inherent complexity of these rocks and its constituents complicates the extraction of representative material parameters such as the reduced elastic modulus (E_r) and hardness (H) for organic matter (OM) via nanoindentation. The present study aims to extract the representative H and E_r values for OM within an over-mature sample set (1.33–2.23%Rr) from the Chinese Songliao Basin and evaluate influencing factors of the resulting parameters. This was realized by means of high-speed nanoindentation mapping in combination with comprehensive optical and high resolution-imaging methods. The average E_r and H values for the different particles range from 3.86 ± 0.17 to 7.52 ± 3.80 GPa and from 0.36 ± 0.02 to 0.64 ± 0.09 GPa, respectively. The results were subsequently processed by the unsupervised machine learning algorithm *k*-means clustering in order to evaluate representative E_r and H results. The post-processing suggests that inherent heterogeneity of OM is responsible for considerable data scattering. In fact, surrounding, underlying and inherent mineral matter lead to confinement effects and enhanced E_r values, whereas cracks and pores are responsible for a lowered stiffness. Adjusted for these influencing factors, a declining trend with increasing maturity (up to 1.96%Rr) could be observed for E_r, with average values calculated from representative clusters ranging from 5.88 ± 0.37 down to 4.07 ± 0.32 GPa. E_r slightly increases again between 2.00 and 2.23%Rr (up to 4.85 ± 0.35 GPa). No clear relationship of H with thermal maturity was observed. The enhanced accuracy archived by a large data set facilitated machine learning approach not only improves further modelling attempts but also allows insights of impacting geological processes on the material parameter and general understanding of mechanical behavior of OM in rock formations. Thus, the presented multimethod approach promotes a fast and reliable assessment of representative material parameters from organic rock constituents.

1. Introduction

In 1992, Oliver and Pharr developed an instrumented nano-indentation method which enables local mechanical material characterization at the micro- and nanometer scales (Oliver and Pharr, 2004, 1992). Since then, this technique has been continuously developed for use with a wide range of engineering (Hay, 2009; Oliver and Pharr, 2010, 2004) and biological materials (Ebenstein and Pruitt, 2006; Oyen, 2013). In recent years, nanoindentation also caught the attention of geoscientists, as the small required testing volume allows the small-scale analysis of highly inhomogeneous rock samples with complex composition and microstructure (e.g., Goldsby et al., 2004; Kranjc et al., 2016;

Ma et al., 2020; Shukla et al., 2015; Thom and Goldsby, 2019; Yin and Zhang, 2011; Zhu et al., 2007). These include for example fine-grained and OM-rich sedimentary rocks (e.g., shales) (e.g., Abedi et al., 2016; Bennett et al., 2015; Bobko and Ulm, 2008; Kumar et al., 2012b, 2015; Liu et al., 2016, 2018; Luo et al., 2020; Ma et al., 2020; Misch et al., 2018; Shukla et al., 2013; Ulm and Abousleiman, 2006; Yang et al., 2020), which not only play a vital role as fossil energy carriers given sufficient thermal maturity, but also represent potential disposal sites for nuclear waste material and may act as geological barriers in the attempt to store anthropogenic CO_2 or H_2 in abandoned hydrocarbon fields (Charlet et al., 2017).

Generally, the mechanical parameters (hardness *H*, elastic modulus *E*) of shales are measured by static or dynamic macro-scaled experiments on drill cores or core plugs. However, while drill core material from exploration wells is generally limited, shale intervals are rarely cored and typically show a poor core recovery and preservation (Kumar et al., 2012b; Liu et al., 2016). Furthermore, the standard macroscopic testing routines often exhibit low precision and inconsistency of results in case of shales, and material properties for the individual constituents (e.g., the organic fraction) cannot be derived either. OM occurs as finely dispersed, layered or network-like varieties and often fills intergranular voids within the rock matrix. This reportedly has a large influence on the mechanical and fracture behavior of the overall rock (Khatibi et al., 2018; Kumar et al., 2015; Sayers, 2013), and therefore on the hydrocarbon producibility and wellbore stability. As a consequence, various studies targeted the nanomechanical characterization of OM in shales using atomic force microscopy (AFM) (Ahmadov et al., 2009; Eliyahu et al., 2015; Emmanuel et al., 2016; Yang et al., 2017) or nanoindentation (Alstadt et al., 2016; Kumar et al., 2012a; Mashhadian et al., 2018; Zeszotarski et al., 2004; Zhao et al., 2020). The large discrepancies between results from both techniques highlight the difficulties in the acquisition of representative material parameters for different OM types. Eliyahu et al. (2015) concluded in their AFM study that the elastic modulus of OM is heterogenous at the nanoscale and that the spatial resolution is a key factor for a full mechanical characterization. However, even at the nanoscale, a precise determination is challenging due to the complex nature of OM particles embedded within the mineral matrix. Individual indents are not sufficient for a holistic mechanical characterization of OM, since the individual particles are restrained by the surrounding fine grained matrix minerals, which affects the nanoindentation response and complicates the mechanical characterization. In contrast, the nanoindentation mapping technique (Bobko and Ulm, 2008; Constantinides et al., 2006; Liu et al., 2018; Luo et al., 2020; Ulm and Abousleiman, 2006) offers great advantages compared to the traditional, individual point measurements. In nanoindentation mapping, material parameters can be obtained statistically from defined equal-distance grids placed on the selected surface areas of interest (e.g., Constantinides et al., 2006; Liu et al., 2018; Ulm and Abousleiman, 2006). By doing so, inherent property variations are captured and interface effects are visualized.

In order to test the suitability of high-speed nanoindentation mapping for the determination of phase-specific micromechanical properties in shales and other OM-rich rocks, various types of OM within a set of samples from a deep exploration well (Songke-2 Well; SK-2) in the Chinese Songliao Basin were characterized. This study is intended as a proof-of-concept for nanoindentation mapping of organic matter in fine-grained rocks of any kind. In order to study the influence of microstructural heterogeneities (e.g., pore structure, surface features, microtexture) on the accuracy of micromechanical data, complementary high-resolution imaging by means of scanning electron microscopy (SEM) and helium ion microscopy (HIM) was conducted. In addition, traditional optical petrography was performed for a clear identification of OM types (kerogen vs. solid bitumen). Cross-correlation between different characterization techniques is a challenge often encountered in shale studies (Hackley et al., 2017). To even enable a spatially-resolved, correlative analysis between the mechanical property maps and the

obtained optical and high-resolution SEM and HIM images, a novel, high-precision marking tool was utilized. Analysis grids were applied by a thermally non-invasive femtosecond laser (Pfeifenberger et al., 2017). This approach vastly improved data correlation and interpretation. Finally, the micromechanical testing results were further processed by the unsupervised machine learning algorithm *k*-means clustering (Hartigan and Wong, 1979). The implementation of the *k*-means clustering served to evaluate phase heterogeneities and grain boundary effects and to identify outliers caused by unavoidable measurement errors in heterogeneous structures. Various material science studies already demonstrated the potential of machine learning application for material characterization as *k*-means proved to be a successful tool for data deconvolution and analysis of nanoindentation results (e.g., Konstantopoulos et al., 2020; Koumoulos et al., 2019; Vignesh et al., 2019). The established work flow for a reliable determination of phase-specific micromechanical properties should improve the quality of input data in digital rock modelling and prediction of rock mechanical changes during subsurface processes such as hydraulic fracturing. Furthermore, using this procedure thermal maturity effects on OM properties are discussed.

2. Material and methods

2.1. Sample material

The examined samples (Table 1) were recovered from the SK-2 well drilled during the Deep Continental Scientific Drilling Engineering Project in the Songliao Basin of Northeastern China. The Songliao Basin covers an area of 260,000 km^2 and is known as one of the most productive oil and gas provinces worldwide (Desheng et al., 1995). Remarkably, the SK-2 well was the deepest continental scientific drilling project accomplished by any Asian nation (Hou et al., 2018). A focus of the project was the exploration of deep unconventional gas resources within the Cretaceous succession. The studied samples were recovered from the Lower Cretaceous Shahezi Formation. These rocks are characterized by a high total organic carbon content (TOC) and extensive occurrences of shale gas (Hou et al., 2018). As the samples originate from great burial depths (3376–4426 m), the present OM is thermally mature. The vitrinite reflectance values range between 1.33 and 2.23% Rr corresponding to the oil phase-out to dry gas transition (Noah et al., 2020). A detailed regional geological overview is given in Hou et al. (2018).

2.2. Sample preparation and laser-marking

Prior to experiments, the selected SK-2 samples were embedded into epoxy resin perpendicular to their bedding plane and mechanically polished (final polishing step: 0.04 μm colloidal SiO_2 suspension with water and polyethylenglykol). The OM within the polished sections were then examined and defined by optical microscopy using Leica DM 4500P

Table 1
Overview of burial depths, vitrinite reflectance values and geochemical bulk parameters by Noah et al. (2020) for the studied samples. (*VR* – vitrinite reflectance, *TOC* – total organic carbon, *S1* – free hydrocarbons (*HC*), *Tmax* – Rock Eval temperature of maximum *HC*-generation, *HI* – hydrogen index).

Name	Depth	VR	TOC	S1	T_{max}	HI
	m	%Rr	wt%	mg HC/g	°C	mg HC/g TOC
SK2	3376	1.33	20.4	0.55	510	56
SK5	3466	1.68	2.42	0.06	533	22
SK9	3586	1.96	7.37	0.05	552	25
SK10	3616	1.89	1.85	0.02	557	17
SK12	3676	2.00	1.31	0.01	555	16
SK18	3866	2.23	4.43	0.02	579	11
SK37	4426	2.21	1.10	0.03	597	5

and DM 4P microscopes, both under oil immersion (DM 4P) and at air in dry state (DM 4500P). Representative areas of interest were selected and subsequently marked with a femtosecond laser-machined grid in order to facilitate nanoindentation and subsequent correlated examination of the OM particles (Fig. 1). The suitability of this ultrashort pulsed laser ablation technique for use with heat-sensitive specimen such as bio-materials is well documented and the thermal overprint is considered negligible (Jakob et al., 2017; Pfeifenberger et al., 2019, 2017). The parameter set used during grid preparation with the Auriga Laser plat-form (Carl Zeiss) is summarized in Table 2.

2.3. High-speed nanoindentation mapping

The nanoindentation property mapping was performed using a Hysitron TS 77 Select (Bruker) equipped with a Cube Corner diamond tip. A fused silica standard was used for the calibration of the Cube Corner area function following the Oliver-Pharr method (Oliver and Pharr, 1992). Prior and subsequently to property mapping, scanning probe microscopy (SPM) was performed to identify and document un-disturbed areas for representative measurements. All SPM images are visualized with Gwyddion (Nečas and Klapetek, 2012). The individual indents were performed in load-controlled mode with a trapezoidal loading profile (0.5 s loading, 1 s hold, 0.5 s unloading) and a maximum load of 800 μN. Equivalent to conventional nanoindentation tests, hardness (H) and reduced elastic modulus (E_r) are calculated based on the evaluation of the resulting load-displacement curves after the Oliver-Pharr method (Oliver and Pharr, 1992). The elastic Young's modulus differs from the reduced elastic modulus mainly in that the deformation of the diamond tip during the testing procedure is considered. For soft material such as OM, the Young's modulus and reduced elastic modulus values are alike, as the deformation of the Cube Corner tip by the soft substrate is negligible. Consequently, in this study E_r will be used as mechanical parameter of OM. For each sample, at least five maps with variable arrays (up to 9×9 indents) were placed on OM particles visible within the femtosecond laser grids. The array spacing was 2–3 μm
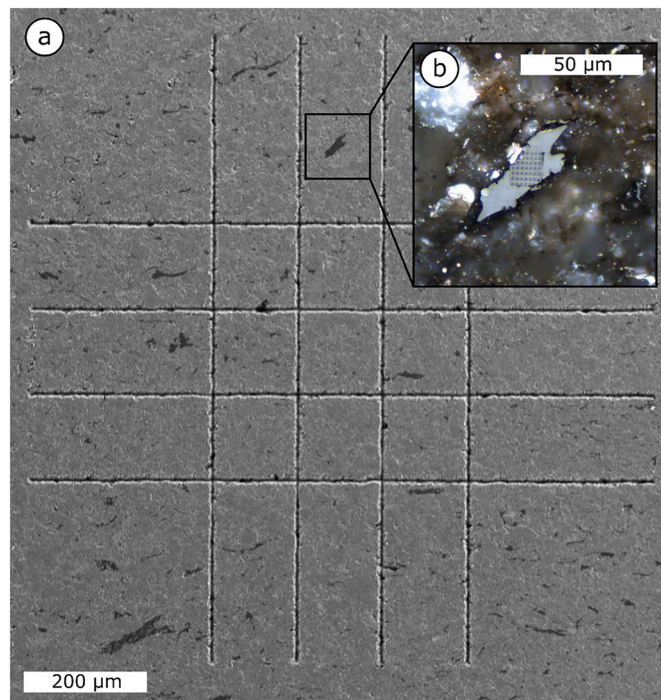
Fig. 1. (a) SEM overview image of a femtosecond laser marked surface of sample SK10, facilitating the (b) optical examination of specific OM particles as well as the nanoindentation mapping of the latter (nanoindentation grid is visible on the surface of the OM particle).

Table 2
Femtosecond laser parameter set for grid preparation (E_f – fluence, f – pulse repetition rate, D – divisor, v_s – scan speed, λ – Laser wavelength, L – line repetitions, S – scan repetitions, for further information see Pfeifenberger et al. (2017)).

E_f	f	D	v_s	λ	L	S
J cm^{-2}	kHz		mm/s	nm		
0.49–1.15	50	15–50	1	515	1	15–25

between the individual measurement spots in order to fully resolve property heterogeneities while still avoiding interference between the indents. An indent-depth ratio of 10 was recommended for a wide va-riety of materials (Sudharshan Phani and Oliver, 2019). Due to the ductile nature of OM resulting in indentation depths of ~700 nm, this ratio is not reached for the studied samples, as such a wide spacing would hinder the correct acquisition of true property heterogeneities. A careful examination of all load-displacement curves for unwanted ef-fects of plastic pre-deformation did not reveal any signs of measurement-induced bias.

2.4. Scanning electron microscopy

Scanning electron microscopy was performed using a Tescan Clara field emission (FE)-SEM equipped with backscattered (BSE) and sec-ondary electron (SE) detectors as well as an energy-dispersive X-ray (EDX) detector (Oxford Instruments). For the correlative study, SEM images were acquired in two steps. At first, imaging was done on the mechanically polished and laser-marked blocks for an overview of measurement spots. These investigations were performed on the un-coated specimen surfaces at low electron energy (<5 kV) in order to maintain the undisturbed state for further introduced HIM imaging. In the second stage (after nanoindentation and HIM), representative sub-specimens were cut from the mechanically polished blocks and further prepared with a Hitachi ArBlade 5000 broad ion beam (BIB) preparation system with an Ar beam at 8 kV for 2 h. The BIB-polished surface was then coated with few nm Au and subsequently imaged at 5–10 kV. BIB-SEM is nowadays a standard technique in the characterization of OM nanostructures, allowing for the investigation of artefact-free micro-structures and particularly porosity associated with OM at high resolu-tion (Hackley et al., 2021).

2.5. Helium ion microscopy

HIM was carried out using an Orion Plus microscope (Carl Zeiss). HIM images were acquired at an acceleration voltage of 34.5–36.1 kV and a beam current set at 0.3–2.9 pA. The sample surface was not sputtered with a conductive layer to prevent artifacts that may result from such coating. Thus, an electron flood gun was used during imaging in order to stabilize charging of the specimen surface. HIM has the capability to provide SE images at ultra-high resolution, and offers a surface sensitivity and contrast superior to conventional FE-SEM. Furthermore, it is particularly efficient in the use with materials constituted of low-mass elements such as carbon, as the helium ion beam has a lower interaction volume compared to an electron beam (Bell, 2009; Hlawacek et al., 2014; Scipioni et al., 2009; Sijbrandij et al., 2010; Ward et al., 2006). Due to the very limited availability of such micro-scopes, relatively few studies have used HIM for the characterization of OM in mudstones and shales (Cavanaugh and Walls, 2016; Hackley et al., 2021; Huang et al., 2020; King et al., 2015; Peng et al., 2015; Wang et al., 2020; Wu et al., 2020). Nevertheless, HIM proved to be a valuable complementary method in this study due to its ability to ach-ieve highest resolutions on mechanically polished and native samples, as well as to better resolve topographic features compared to SEM (Cav-anaugh and Walls, 2016; King et al., 2015).

2.6. k-means clustering

k-means is a machine learning algorithm for cluster analysis. It identifies the local means of a given number of cluster subsets *k* within a larger dataset. After predefinition of the number of clusters *k*, the algorithm optimizes the clustering by assigning each data point to the cluster with the closest mean central value ("centroid") (Hartigan and Wong, 1979). The clustering is then iteratively improved until the average sum of squared distances amid points of each cluster is minimized and no further point shifts occur (Hartigan and Wong, 1979). *k*-means clustering is classified as unsupervised machine learning since labeling, categorization and training of the data set prior to analysis is not required. However, the number of clusters needs to be predetermined by the users, either by knowledge of the phases within the sample (Vignesh et al., 2019) or by the implementation of heuristic methods for quality validation of clustering. These approaches include for instance the Elbow method (Thorndike, 1953) and the Silhouette method (Rousseeuw, 1987). After specifying the number of clusters, the initial centroids are chosen uniformly at random, then recomputed iteratively until the minimal within-cluster sum of squares is reached. However, this random initialization might affect overall clustering performance for certain data sets. Implementation of the *k*-means++ algorithm (Arthur and Vassilvitskii, 2007) is an approach for improved cluster initialization and was adopted for this study. Property mapping results for *H* and *E_r* were clustered using the Python machine learning library scikit-learn (Pedregosa et al., 2011) in order to improve local mean values for the individual mapped phases and to detect boundary effects. The clustering algorithm was applied twice on each data set: (1) the tested minerals were separated from the OM within the map in order to (2) evaluate the different mechanical domains within the OM particles.

3. Results

3.1. Optical and SEM petrography

Optical and scanning electron microscopy revealed strongly differing textural characteristics of the imaged samples. The following description is ordered according to increasing burial depth and thermal maturity (see Table 1).
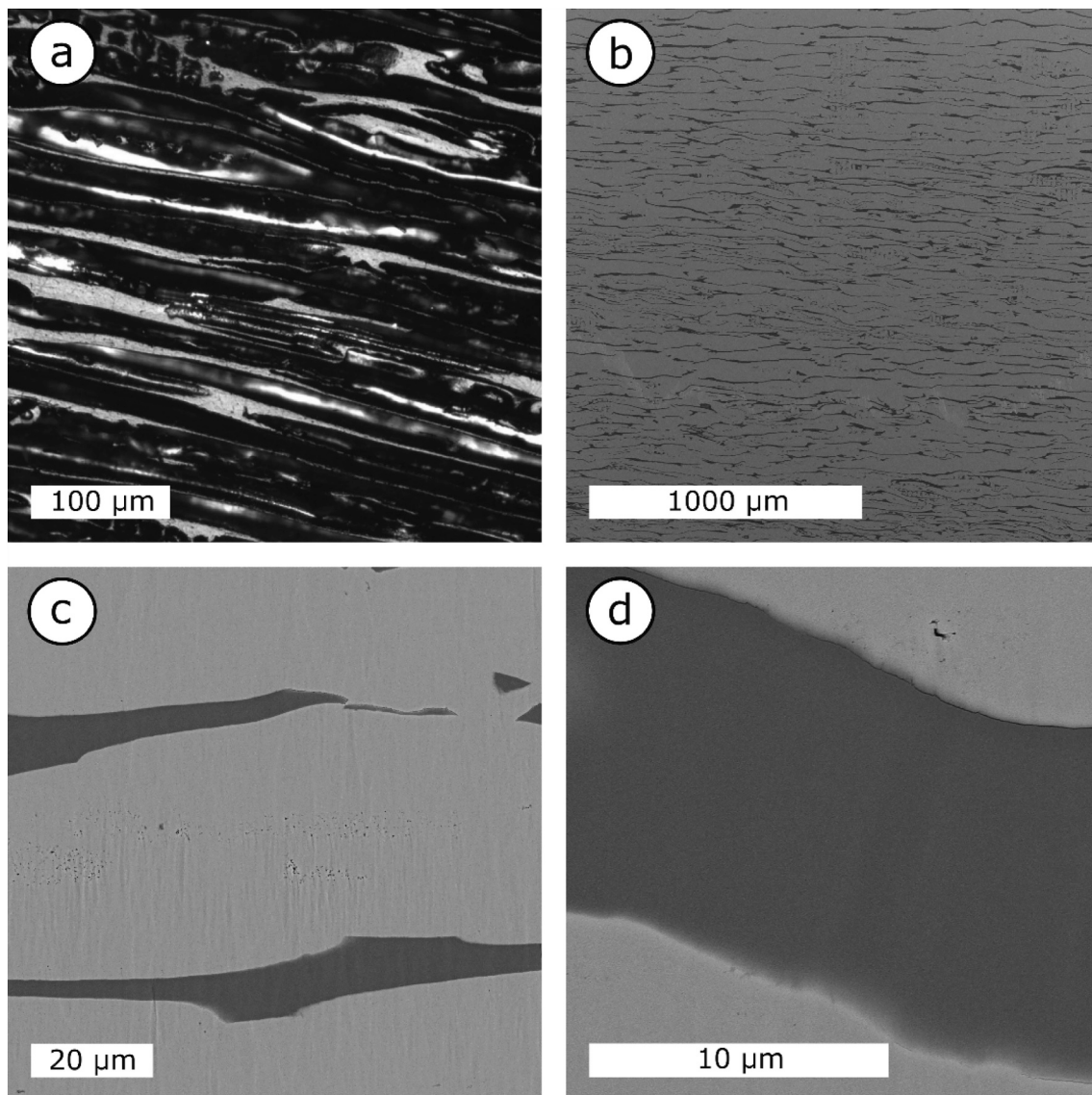

Fig. 2. (a) Optical image (oil immersion) of sample SK2 showing elongated vitrinite particles. (b) BSE overview image of the BIB polished area. (c, d) Non-porous OM within chert exhibiting occasional pores.

3.1.1. SK2

Sample SK2 (1.33%Rr) consists of silicified fossil wood with abundant vitrinite (Fig. 2a). The well-preserved cell structure, which is also visible in the BSE overview image (Fig. 2b), indicates that silicification occurred during early diagenesis. Due to the dilution by microcrystalline quartz (chert), the TOC content is only ~20 wt% (Table 1). Nevertheless, SK2 is the most organic matter-rich of all studied samples. The elongated OM parts appear structureless and non-porous at higher BIB-SEM resolution (Fig. 2c, d). The chert exhibits occasional pores, which are frequently located in proximity to vitrinite (Fig. 2d). However,
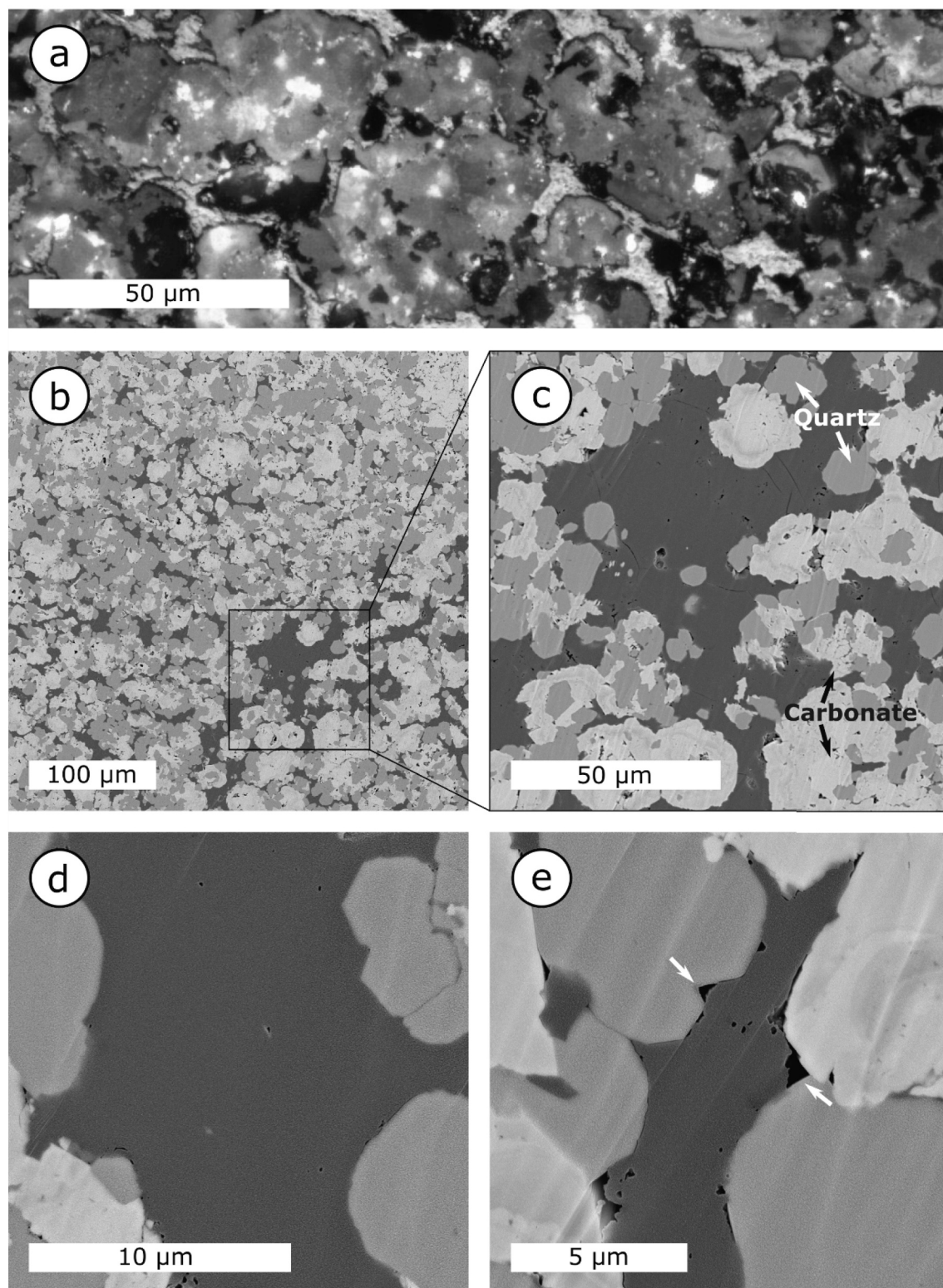

Fig. 3. (a) Photomicrograph of the solid bitumen network in sample SK5. (b) BIB-SEM overview of the OM network filling intergranular voids in-between carbonate and quartz grains; the detail image in (c) shows porous bitumen hosting round and angular pores and quartz inclusions. (d) Solid bitumen containing few pores. (e) Porous solid bitumen with large interface pores (white arrows).

overall porosity is limited in the microcrystalline quartz as well.

3.1.2. SK5

Sample SK5 (1.68%Rr) hosts solid bitumen filling intergranular pore space in-between coarse quartz and carbonate grains (Fig. 3a). The solid bitumen forms a continuous OM network throughout the imaged specimen (Fig. 3b–e). In contrast to sample SK2, vitrinite is largely absent. OM pores are generally rare but occur occasionally within the solid bitumen groundmass or at interfaces with matrix minerals (Fig. 3c–e). These pores exhibit either rounded or angular morphologies.

3.1.3. SK9, SK10, SK12

Samples SK9 (1.96%Rr), SK10 (1.89%Rr) and SK12 (2.00%Rr) show similar thermal maturity and OM types, SK9 is richest in OM (7.37 wt% TOC; Table 1). In contrast to the comparable OM composition, the mineral matrix texture of the three samples varies considerably (Figs. 4b, 5b, 6b). Sample SK9 is characterized by large grains and considerable carbonate cementation (Fig. 4b), while SK10 is dominated by fine-grained clay minerals (Fig. 5b). Sample SK12 is characterized by a clay matrix similar to sample SK10, but coarse grains and carbonate-cemented areas are also present (Fig. 6b).

All three samples are characterized by relatively large, disseminated vitrinite particles, while inertinite occurs in smaller amounts (Figs. 4a, 5a, 6a). BIB-SEM images reveal that the structureless OM is non-porous (Figs. 4c, d, 5c, 6d). However, particularly in samples SK10 and SK12, OM particles with significant amounts of finely dispersed mineral inclusions were observed (Figs. 5d, 6c).

3.1.4. SK18, SK37

Samples SK18 (2.23%Rr) and SK37 (2.21%Rr) are the specimen with the highest maturity. Sample SK18 (4.43 wt% TOC; Table 1) contains a shaly part with detrital vitrinite particles and an approximately 5 mm thick vitrinite layer.

One large detrital vitrinite particle in the shaly part contains abundant authigenic quartz (Fig. 7a–c), while authigenic quartz in the thick vitrinite band occurs less frequently (Fig. 7d, e). Vitrinite contains occasional pores, which are mostly angular and occur in irregularly distributed clusters often adjacent to the authigenic minerals.

Sample SK37 has the lowest TOC content of all studied samples and consequently exhibits a low amount of OM particles (Fig. 8a, c). The observed OM is mostly vitrinite and inertinite, embedded into a clay mineral-rich matrix (Fig. 8c, d). Only few vitrinite particles host minor internal porosity (Fig. 8b).

3.2. High-speed nanoindentation mapping and correlative high-resolution imaging

High-speed nanoindentation mapping was performed for 38 selected OM particles within the investigated samples (Table 1). The average E_r and H values of all maps are summarized in Table 3. Additionally, the total average of all maps from each sample were calculated for a better comparability (Table 4).

Seven maps have been collected for vitrinite in sample SK2 (1.33% Rr). The average E_r values for these maps range from 5.85 to 6.77 GPa, resulting in the highest total average E_r value of all samples (6.26 ± 1.09 GPa). The average H values vary from 0.45 to 0.57 GPa. Variations within a particle and the respective load-displacement curves are displayed for a vitrinite grain (map 5) in SK2 (Fig. 9).

Five maps representing solid bitumen were obtained for sample SK5 (1.68%Rr). Both average E_r (4.98–5.81 GPa) and H (0.40–0.48 GPa) values are lower than for vitrinite in SK2.

Five vitrinite particles were selected from sample SK9 (1.96%Rr). Four of these particles (maps 2–5) show relatively low average E_r (3.86–4.68 GPa) and H values (0.36–0.48 GPa). The lowest deviation of E_r and H values within a map in SK9 were obtained from a relatively large and homogenous vitrinite particle (map 5) (Fig. 10). Only map 1 exhibits a higher average E_r of 6.65 ± 1.71 GPa, likely due to abundant authigenic minerals. However, in contrast to E_r, the average H value of map 1 (0.46 ± 0.04 GPa) is within the range of the other vitrinite particles.

Five vitrinite particles (maps 1–5) in sample SK10 (1.89%Rr) are characterized by higher average E_r (4.83–6.34 GPa) and H values (0.47–0.54 GPa) compared to SK9, despite of the comparable thermal maturity of both samples.

The average E_r obtained from five vitrinite particles (maps 1–5) in sample SK12 at 2.00%Rr are rather uniform (4.83–4.98 GPa). They range above most of the values determined in SK9, but lower compared to SK10. The average H values span from 0.39 to 0.54 GPa.

Six vitrinite maps were obtained for sample SK18 (2.23%Rr). Maps 1 to 3 represent the approximately 5 mm-thick coaly layer described above and display relatively consistent average E_r (4.64–4.91 GPa) and H values (0.54–0.57 GPa). Maps 4 to 6 represent vitrinite particles in the shaly part of the sample and show slightly higher E_r values (5.04–7.52 GPa). The high average E_r value of map 4 is also characterized by a large standard deviation (7.52 ± 3.8 GPa). Average H values in the range of 0.50 to 0.57 GPa are similar to those in the coaly layer.

One inertinite (map 1) and four vitrinite particles (maps 2–5) were investigated in sample SK37 (2.21%Rr). Average E_r and H values obtained from the vitrinite maps range from 4.67 to 5.61 GPa and from 0.49 to 0.59 GPa, respectively. The inertinite particle exhibits an average E_r of 5.65 ± 2.7 GPa which is similar to that of vitrinite in map 4, but its H value (0.64 ± 0.09 GPa) is the highest of all investigated OM particles.

The total average E_r and H values obtained of each sample (average of all maps per sample, see Table 4) are plotted versus vitrinite reflectance in Fig. 11. The plot reveals a large variation for the mechanical parameters, in particular for E_r (see Fig. 11). Based on the average E_r (Table 4), a slight decrease with increasing maturity can be observed. In contrast, the average H values vary from 0.40 to 0.56 GPa without a systematic maturity trend.
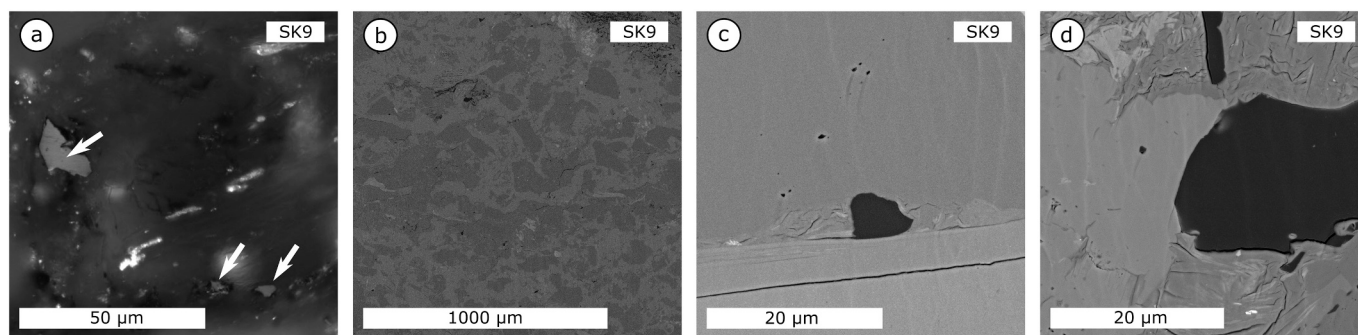

Fig. 4. Photomicrograph and BIB-SEM images of sample SK9. (a) Optical image of vitrinite particles (white arrows) under oil immersion. (b) BIB-SEM overview of the rock texture. (c, d) BIB-SEM images of non-porous OM particles.
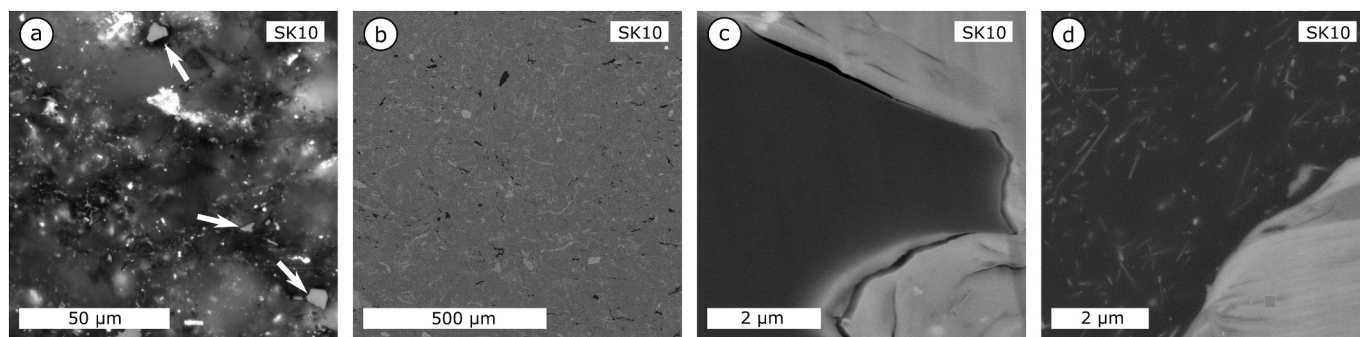
Fig. 5. (a) Optical image of vitrinite particles (white arrows) under oil immersion within sample SK10. BIB-SEM images displaying an (b) overview of the mineral fabric, (c) non-porous OM particle and (d) OM hosting finely dispersed mineral inclusions.
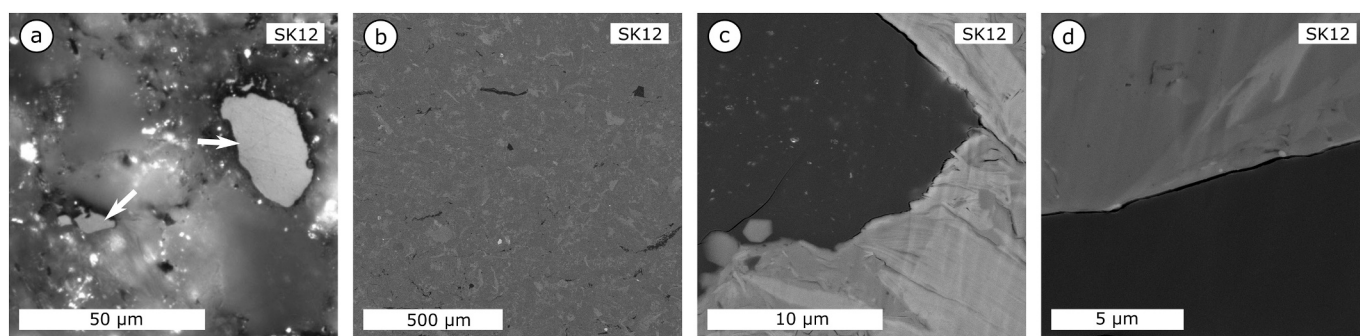

Fig. 6. (a) Photomicrograph displaying vitrinite particles in sample SK12. (b) BIB-SEM overview of the sample. (c) OM particle containing mineral matter. (d) BIB-SEM images of a non-porous OM particle of sample.

Fig. 12a shows an optical micrograph of a vitrinite particle in sample SK12 (map 4). The correlative HIM image of the OM particle is presented in Fig. 12b. Nanoindents are shown in the SPM surface map (Fig. 12c). HIM imaging revealed that the SPM surface scans affected the soft maceral surface (Fig. 12d, detail in D). Corresponding property maps for E_r and H are displayed in Fig. 12e, where the highest E_r values are observed in proximity to mineral grain boundaries.

A further example of nanoindentation property mapping of a vitrinite particle is shown for sample SK12 in Fig. 13 (Table 3, map 5 in SK12). HIM imaging enabled a more detailed view on individual indents and cracks within the OM (see inset in Fig. 13a). The property maps exhibit local variability of E_r and (at a lesser degree) H values and in combination with the correlative imaging it appears, that these are often obtained in proximity to surrounding mineral matrix and cracks (Fig. 13 a, b). E_r values of OM adjacent to minerals are typically enhanced, but reduced values were also obtained (Fig. 13b). In order to correct for such unwanted boundary and topography effects, k-means clustering was executed on the micromechanical dataset in order to obtain "representative" OM properties (see explanations below).

3.3. k-means clustering

k-means clustering was applied on the mapping datasets in order to study the data structure by identifying clusters and their centers (Fig. 14a). The maximum number of clusters was set to four. These different clusters within an individual OM particle may represent influencing factors such as proximity to mineral grain boundaries (Fig. 14b, c) or the local presence of pores or cracks. For several samples, the Elbow method (Thorndike, 1953) and the Silhouette method (Rousseeuw, 1987) proved helpful in predetermining the cluster number. The final assignment of clusters and the quality check of individual measurements was assisted by the evaluation of SPM maps and, if available, data from correlative high-resolution imaging (Figs. 12, 13).

Usually, the most "representative" OM domains (no apparent mineral inclusions/pores/cracks; distant to grain boundaries) are represented by the largest clusters for most property maps (Figs. 14, 15). The remaining obtained clusters and their respective centroids are denominated as "low", "elevated" and "high" based on their values compared to the "representative" clusters/centroids (Table A in supplemental). In contrast to map 1 in sample SK2 (Fig. 14), map 1 in SK10 also needs to be corrected for a "low" cluster, underestimating the representative results (Fig. 15; Table A in supplemental).

Table A (see supplemental to this article) summarizes the k-means clustering results for E_r and H values obtained from each property map. In order to ensure reliability and enable comparability between the samples, the average of all data points within the representative clusters per sample/vitrinite reflectance were calculated (Table 5). Average representative k-means E_r show a decreasing trend with increasing vitrinite reflectance (Fig. 16a) from 1.33 up to 1.96%Rr. In contrast, no maturity trend exists for the average k-means H (Fig. 16b), which remains relatively constant for all samples (0.40–0.55 GPa).

OM at 1.33%Rr (SK2) exhibits the highest E_r with representative k-means centroids ranging from 5.41 to 6.17 GPa (seven maps, mean at 5.88 $\pm$ 0.37 GPa calculated from data points within representative clusters). For solid bitumen in SK5 at 1.68%Rr the representative k-means centroids for E_r vary from 4.68 to 5.25 GPa. The average E_r calculated from representative clusters for E_r at 1.89%Rr (SK10), 1.96% Rr (SK9) and 2.00%Rr (SK12), obtained from 5 maps each, deviate significantly from each other, despite the minor differences in thermal maturity (Table 5). The largest discrepancy between representative E_r centroids is observed at 1.96%Rr (SK9), where the k-means centroids of four out of five maps show only minor variation from 3.86 to 4.27 GPa, whereas one larger OM layer with mineral inclusions is strongly shifted to 5.58 GPa (Table A in supplemental, map 1 in SK9).

The average representative E_r obtained from samples at ~2.2%Rr range at 4.43 $\pm$ 0.55 GPa for sample SK37 (five maps) and
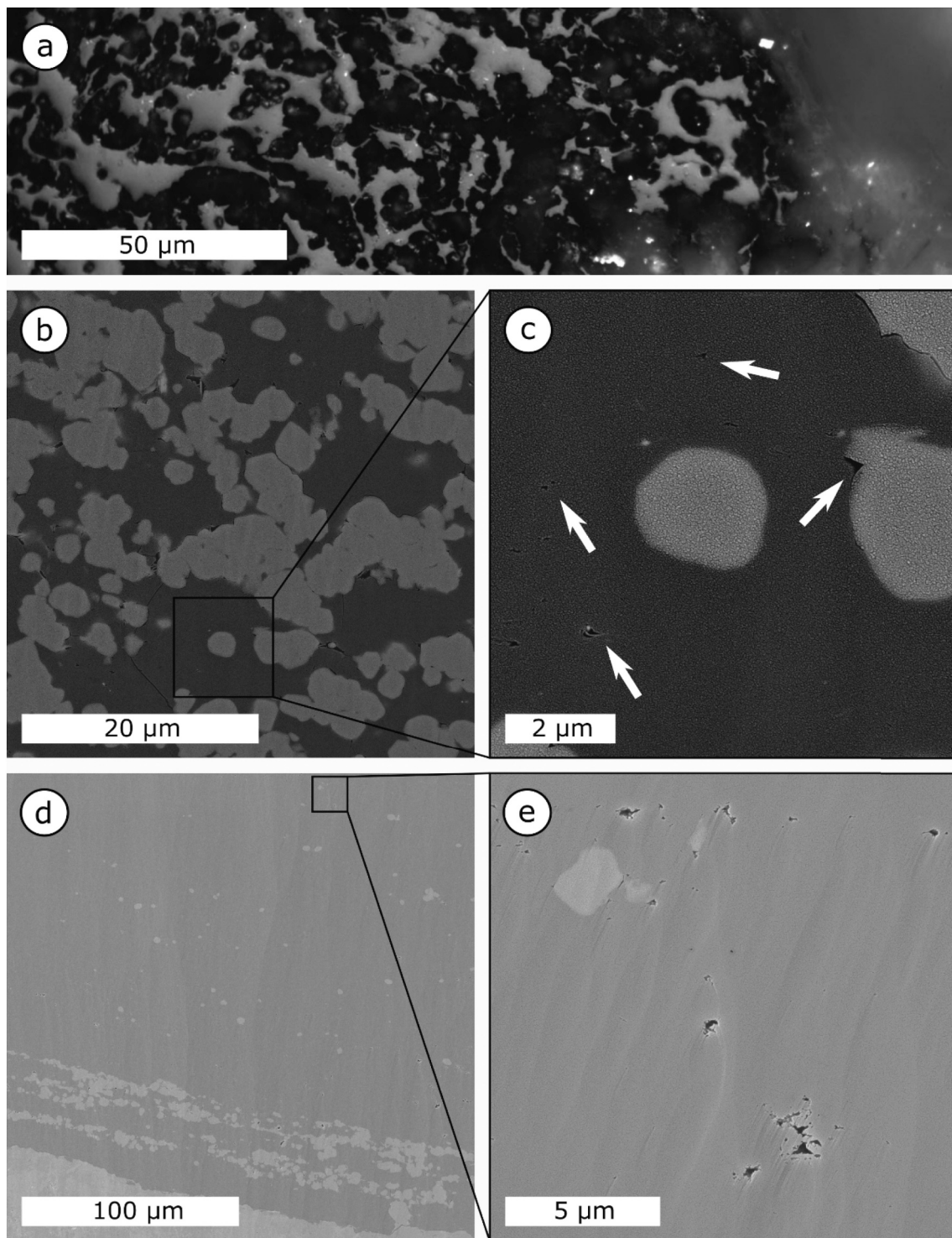
Fig. 7. (a) Optical image (oil immersion) of dispersed vitrinite in sample SK18. (b, c) Porous vitrinite hosting authigenic minerals (predominately quartz). (d, e) BIB-SEM overview and detail images of a broad vitrinite layer hosting angular pores and quartz inclusions.

4.85 ± 0.35 GPa (six maps) for sample SK18. In contrast to the remaining samples, an inertinite particle was also included in the testing of sample SK37, exhibiting similar results compared to vitrinite (Table A in supplemental, map 1 in SK37). The results for SK18 were obtained from six property maps including three maps from a single vitrinite layer and three maps from dispersed vitrinite hosting authigenic minerals. The particles with authigenic mineral inclusions show slightly elevated E_r values and more variation between the individual representative centroids (4.77–5.37 GPa; Table A in supplemental, map 4–6 in SK18)

compared to those obtained from the homogeneous vitrinite layer (4.79–4.83 GPa; Table A in supplemental, map 1–3 in SK18). Furthermore, the non-representative "elevated" and "high" clusters of vitrinites with extensive authigenic mineral occurrence show considerably higher E_r values with a maximum at 16.86 GPa for a non-representative centroid (Table A in supplemental, map 4 in SK18).
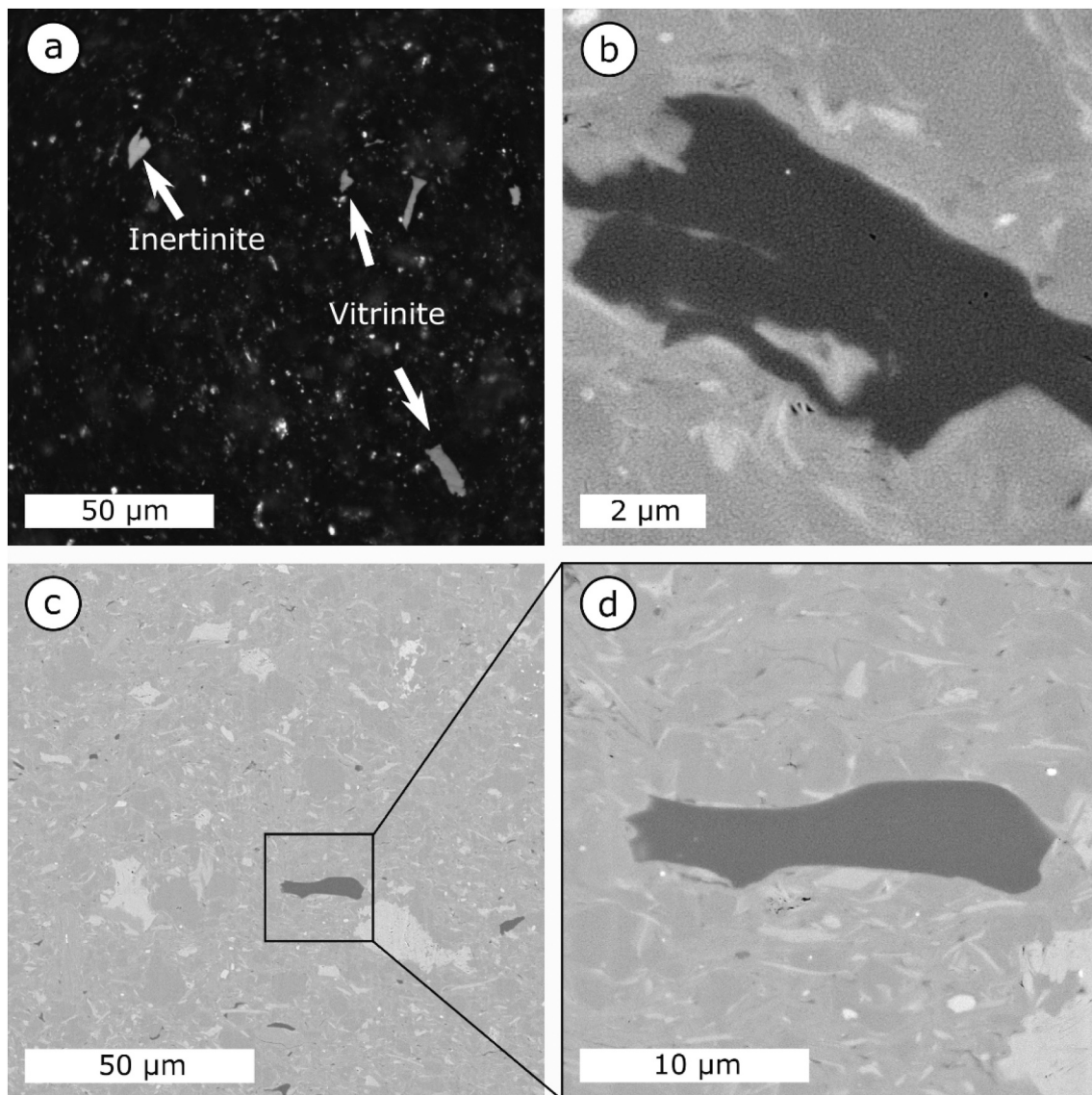
Fig. 8. (a) Photomicrograph of vitrinite and inertinite particles within sample SK37. (b) BSE image of an OM particle exhibiting few internal pores. (c) BIB-SEM overview of SK37 documenting the OM-lean texture with only few isolated OM particles. (d) Detail image of a non-porous OM particle interpreted as vitrinite.

4. Discussion

4.1. Influence of boundary proximity and mineral inclusions on micromechanical properties of organic matter

The nanoindentation property mapping revealed strong heterogeneities of the micromechanical parameters (especially E_r) within individual OM particles. These variations are mostly noticed either in presence of mineral inclusions within OM or the restraint by surrounding mineral grains, mostly resulting in increased elastic modulus values near OM – mineral grain boundary regions (Figs. 12–15). Also, the nanoindentation mapping-procedure might also induce cracks in tested particle (Fig. 17). For the postmature samples investigated here, the locally increased E_r values are interpreted as the result of intense burial compaction and consequently the OM being indented by the grain framework. Similar observations (enhance apparent modulus of OM due to surrounding and underlying mineral matrix) were also reported by Zargari et al. (2016) for OM in Bakken shales.

Vranjes et al. (2018) observed a positive correlation of ash yield (inorganic residue after coal combustion) and the E_r of vitrinite in coals. As the mineral matter content of a coal seam can be approximated by its ash yield, this trend was interpreted as the result of a relative density increase of the tested vitrinite particles due to mineral inclusions.

Even for the undisturbed OM groundmass (representative centroids and respective data points from k-means clustering), significantly different E_r values have been determined for samples at comparable thermal maturity (e.g., samples SK10, SK9 and SK12 at 1.89, 1.96 and 2.00%Rr VR, respectively; Table 5; Table A in supplemental). For these samples, BIB-SEM images reveal substantial differences regarding grain size and diagenetic cementation (Figs. 4b, 5b, 6b). The average E_r obtained from representative k-means clusters for the OM particles within the coarse-grained, well-cemented sample SK9 is 4.07 ± 0.32 GPa (excluding an outlier from mineral matter-rich OM; see Table 5; Table A in supplemental, map 1 in SK9) and ranges considerably lower compared to the finer-grained, clay-rich sample SK10 (average E_r at 5.01 ± 0.34 GPa).

This difference in stiffness is likely attributed to the more intense burial compaction in the clay-rich facies. The absence of pressure shadows in-between large, brittle mineral grains results in a systematic increase in OM compression by the surrounding clay matrix. Enhanced compression might be an effect of more efficient compaction effects based on the plate-like morphologies of clay minerals (Hubbert and

Table 3

Average E_r and H results and corresponding standard deviation (SD) values calculated based on the total number of indents per particle (n) for each map. (v – vitrinite, sb – solid bitumen, i – inertinite).

Name	Map	Average				OM type	n
		E_r	SD	H	SD		
		GPa	GPa	GPa	GPa		
SK2	1	6.77	1.71	0.46	0.05	v	33
	2	5.90	0.80	0.46	0.05	v	40
	3	6.46	1.26	0.45	0.05	v	14
	4	5.85	0.45	0.55	0.02	v	30
	5	6.11	0.97	0.57	0.03	v	58
	6	6.01	0.25	0.53	0.03	v	24
	7	6.76	1.15	0.53	0.06	v	41
SK5	1	5.81	1.51	0.47	0.09	sb	21
	2	5.09	0.52	0.40	0.02	sb	46
	3	4.98	0.73	0.44	0.04	sb	40
	4	5.50	1.35	0.48	0.06	sb	34
	5	5.33	1.27	0.41	0.02	sb	15
SK9	1	6.65	1.71	0.46	0.04	v	24
	2	4.30	0.57	0.48	0.04	v	33
	3	4.28	0.80	0.36	0.02	v	35
	4	4.68	1.12	0.46	0.07	v	18
	5	3.86	0.17	0.36	0.02	v	48
SK10	1	5.20	0.81	0.51	0.02	v	30
	2	5.41	0.44	0.53	0.02	v	39
	3	4.83	0.43	0.47	0.02	v	66
	4	5.72	1.49	0.54	0.05	v	28
	5	6.34	1.76	0.49	0.05	v	27
SK12	1	4.85	1.26	0.47	0.06	v	41
	2	4.98	0.77	0.39	0.03	v	44
	3	4.94	0.57	0.48	0.02	v	37
	4	4.94	1.09	0.49	0.03	v	62
	5	4.83	0.64	0.54	0.03	v	24
SK18	1	4.91	0.18	0.57	0.02	v	22
	2	4.76	0.18	0.55	0.01	v	47
	3	4.64	0.38	0.54	0.01	v	21
	4	7.52	3.80	0.57	0.15	v	22
	5	5.06	0.56	0.56	0.06	v	36
	6	5.04	0.92	0.50	0.03	v	32
SK37	1	5.65	2.70	0.64	0.09	i	39
	2	4.67	1.01	0.52	0.08	v	50
	3	4.98	1.23	0.59	0.05	v	25
	4	5.61	2.07	0.56	0.04	v	25
	5	4.69	0.83	0.49	0.03	v	25

Rubey, 1959; Revil et al., 2002). Hence, the lower clay content and predominately coarse-grained mineral matrix of sample SK9 likely impeded compaction, thereby leading to less confinement and lower average E_r of OM particles (Fig. 10; Table 5).

4.2. Micromechanical changes with thermal maturation and pore structure evolution

The average E_r calculated from the data points within representative

k-means clusters of OM exhibit a decreasing trend with increasing thermal maturity (%Rr). Declining modulus values were also observed by Zargari et al. (2016) for kerogen at maturity levels from the onset of the oil window throughout the gas window. According to these authors, this observation is likely related to the formation of gas- or bitumen-filled nanopores with proceeding thermal maturity. In contrast, Emmanuel et al. (2016) showed in their AFM study a general increase of the elastic modulus for kerogen between 0.40 and 0.82%Rr and stable mechanical properties between 0.82 and 1.25%Rr. A general increase of the Young's modulus of vitrinite with thermal maturity (between 0.62 and 1.13%Rr) was also demonstrated in the nanoindentation study by Zhao et al. (2020). Both studies (Emmanuel et al., 2016; Zhao et al., 2020) concluded that the thermally-induced stiffness increase is likely a result of ongoing aromatization. These findings are supported by an atomistic modelling study where the Young's modulus of kerogen increases exponentially with density and aromatic ordering caused by increasing burial stress (Kashinath et al., 2020). However, the natural variability of OM-hosted porosity was not accounted for in the fundamental property modelling study and the authors emphasize that local porosity may lead to a significant weakening (Kashinath et al., 2020 and references therein). The effects of pore generation have been discussed within a previous TEM study on vitrinite macerals in coals (Vranjes-Wessely et al., 2020). In the aforementioned study, a stiffness decrease has been linked to increasingly larger mesoporosity due to hydrocarbon cracking from the primary kerogen. Vranjes-Wessely et al. (2020) concluded that smaller pores can share an applied load more efficiently in contrast to samples containing fewer but larger pores. It also needs to be emphasized that most experimental data cited for kerogen (Emmanuel et al., 2016; Zargari et al., 2016; Zhao et al., 2020) was obtained from samples below a thermal maturity of 1.25%Rr, whereas the specimen in this study cover postmature samples up to 2.23%Rr. No major SEM-visible OM-hosted porosity was observed in samples at 1.33%Rr, 1.89%Rr, 1.96 and 2.00%Rr. Furthermore, the apparent absence of visible OM porosity at 1.33%Rr (Fig. 2c, d) might be linked to pore occlusion by hydrocarbons (bitumen), as previously demonstrated by bitumen-extraction experiments of post-mature samples (Misch et al., 2019b; Valenza et al., 2013; Wei et al., 2014). In comparison, kerogen at 2.23%Rr (sample SK18) exhibits distinct porosity (Fig. 7c, e) indicating removal of clogging bitumen from pores and further thermally induced pore generation (Misch et al., 2019a). The OM pores at 2.23%Rr are characterized by angular/asymmetrical shapes and inhomogeneous distribution within the particles (Fig. 7c, e). Irregular pore distribution within a single OM particle might be attributed to initial inherent inhomogeneities (Löhr et al., 2015), differential grain support during compaction (Curtis et al., 2012; Mathia et al., 2016; Schieber, 2013) and intercalations between OM and mineral matter (Mathia et al., 2016; Milliken et al., 2013). Misch et al. (2020) showed that OM-hosted pore shapes are influenced by burial compaction similar as mineral matrix pores. A slight increase of the average representative E_r observed from 2.00 to 2.23%Rr might be an indicator of enhanced confinement of the

Table 4

Average E_r and H values for each sample. (v – vitrinite, sb – solid bitumen, i – inertinite).

| Name	Depth	VR	Average				Indents	OM types	Comments
			E_r	SD	H	SD			
	m	%Rr	GPa	GPa	GPa	GPa	n		
SK2	3376	1.33	6.26	1.09	0.52	0.06	240	v	All data included
SK5	3466	1.68	5.27	1.06	0.44	0.06	156	sb	All data included
SK9	3586	1.96	4.19	0.70	0.40	0.06	134	v	Outlier excluded (map 1)
			4.56	1.27	0.41	0.07	158	v	All data included
SK10	3616	1.89	5.35	1.10	0.50	0.04	190	v	All data included
SK12	3676	2.00	4.92	0.94	0.47	0.06	208	v	All data included
SK18	3866	2.23	5.21	1.64	0.55	0.06	180	v	All data included
			4.77	0.26	0.56	0.02	90	v	Coaly part (maps 1, 2, 3)
			5.65	2.23	0.54	0.09	90	v	Shaly part (maps 4, 5, 6)
SK37	4426	2.21	5.09	1.78	0.56	0.09	164	v, i	All data included
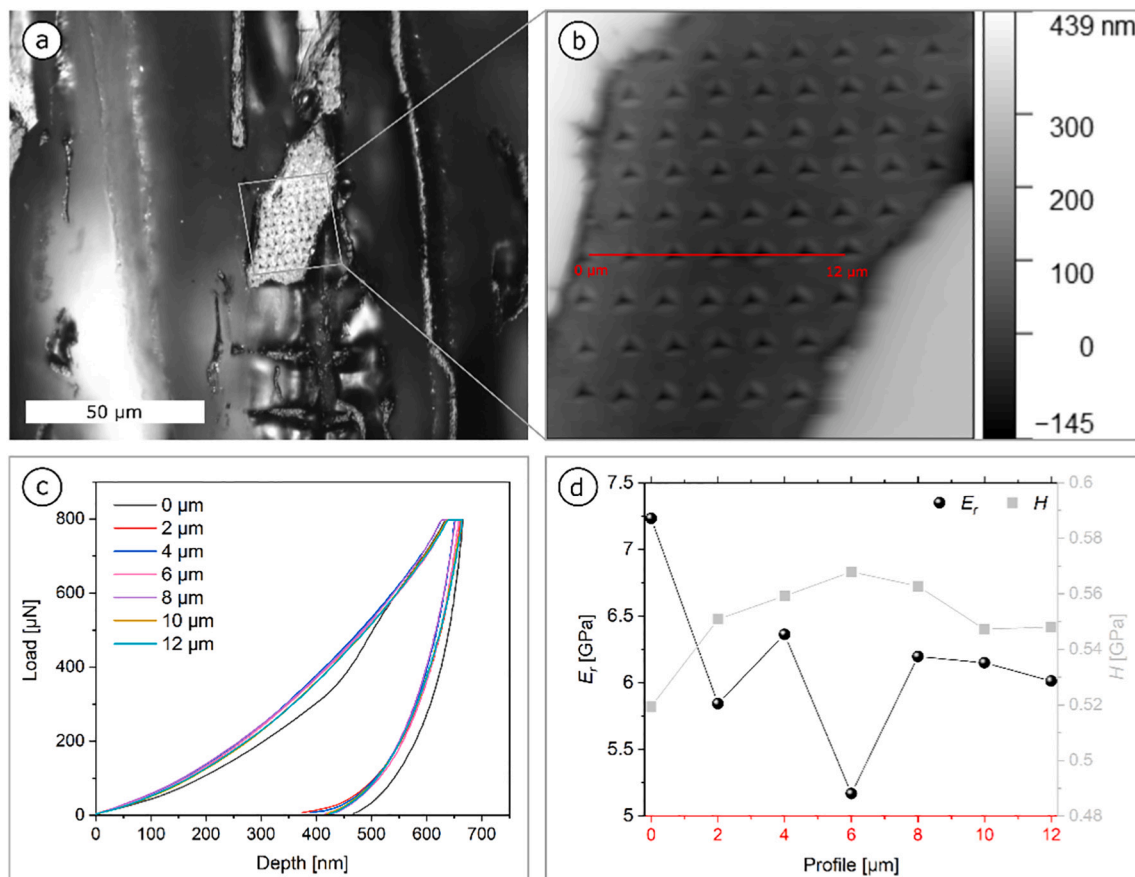
Fig. 9. (a) Photomicrograph of a vitrinite particle (map 5) in sample SK2 under oil-immersion and (b) the corresponding SPM image (20×20 μm scan). (c) Nanoindentation load-displacement curves measured along the profile (red line in (b)) resulting in the respective E_r and H values shown in (d). (For interpretation of the references to color in this figure legend, the reader is referred to the web version of this article.)

particles due to greater burial depth (Fig. 16; Table 5). The virtual absence of SEM-visible porosity likely results from increased confinement effects of OM restrained within the grain framework. A dependence of OM porosity and pore geometry factors on brittle mineral content was also reported by Misch et al. (2018) for oil to wet gas mature shales. In the aforementioned study, abundant OM pores at gas window maturity were interpreted as being the result of lesser compaction in-between a brittle grain fabric. Nevertheless, the visible OM pores within the sample SK5 (Fig. 3c–e) at 1.68%Rr might be rather associated with organic – inorganic interfaces than under-compaction, which is supported by relatively high E_r values despite a porous structure of the investigated OM.

Interestingly, despite the OM tested in SK5 is interpreted as secondary solid bitumen rather than vitrinite, the determined stiffness is among the highest values of all investigated samples (Tables 3–5; Table A in supplemental). Therefore, it is suggested that the controlling factors for micromechanical properties are complex and not solely related to the evolving pore structure. In consequence, the general decrease of E_r with increasing thermal maturity cannot exclusively be assigned to evolving pore development and stiffness prediction therefore requires a comprehensive evaluation of all possible maturity-related geochemical and structural changes, as well as the microstructural characteristics of the individual sample, which in turn controls the porosity preservation (see also Curtis et al. (2012)). Thus, the material properties of OM can be viewed as the result of mechanical and geochemical processes that vary for each unique geological environment. Our novel approach using *k*-means clustering in conjunction with high-resolution imaging techniques has proven to be an effective approach for geological reasoning of micromechanical property variations.

4.3. Micromechanical properties of vitrinite/inertinite versus solid bitumen

Different OM classifications are used in organic geochemical and petrographical studies (see Misch et al., 2019a and Mastalerz et al., 2018). Vitrinite is the predominant OM constituent in the studied sample set (see Figs. 2a, 4a, 5a, 6a, 7a, 8a). The structure of vitrinite is characterized by a great degree of aromaticity, which further increases with thermal maturity. In contrast, solid bitumen, a transformation product of primary OM during thermal alteration, hosts a significant proportion of aliphatic hydrocarbon chains. However, these aliphatic compounds break down with ongoing cracking, resulting in a relative increase of aromaticity (Craddock et al., 2015). This leads to a convergence of the reflectance properties of solid bitumen and vitrinite above 1.0%Rr (Hackley and Lewan, 2018; Landis and Castaño, 1995) and particularly in overmature stage, growing a challenge in their discrimination.

According to previous nanomechanical studies, primary macerals (vitrinite and inertinite) exhibit a higher stiffness compared to more ductile solid bitumen (Emmanuel et al., 2016; Zhao et al., 2020). However, the results of Zhao et al. (2020) indicate that the Young's modulus of solid bitumen increases with thermal maturity and becomes more similar to the values determined for vitrinite at equal maturity beyond the late oil window (see table 2 in Zhao et al. 2020). This is supported by the mechanical parameters determined for solid bitumen in sample SK5 of this study; E_r and H values comparable to vitrinite in the overmature sample are likely a result of the increased aromaticity at
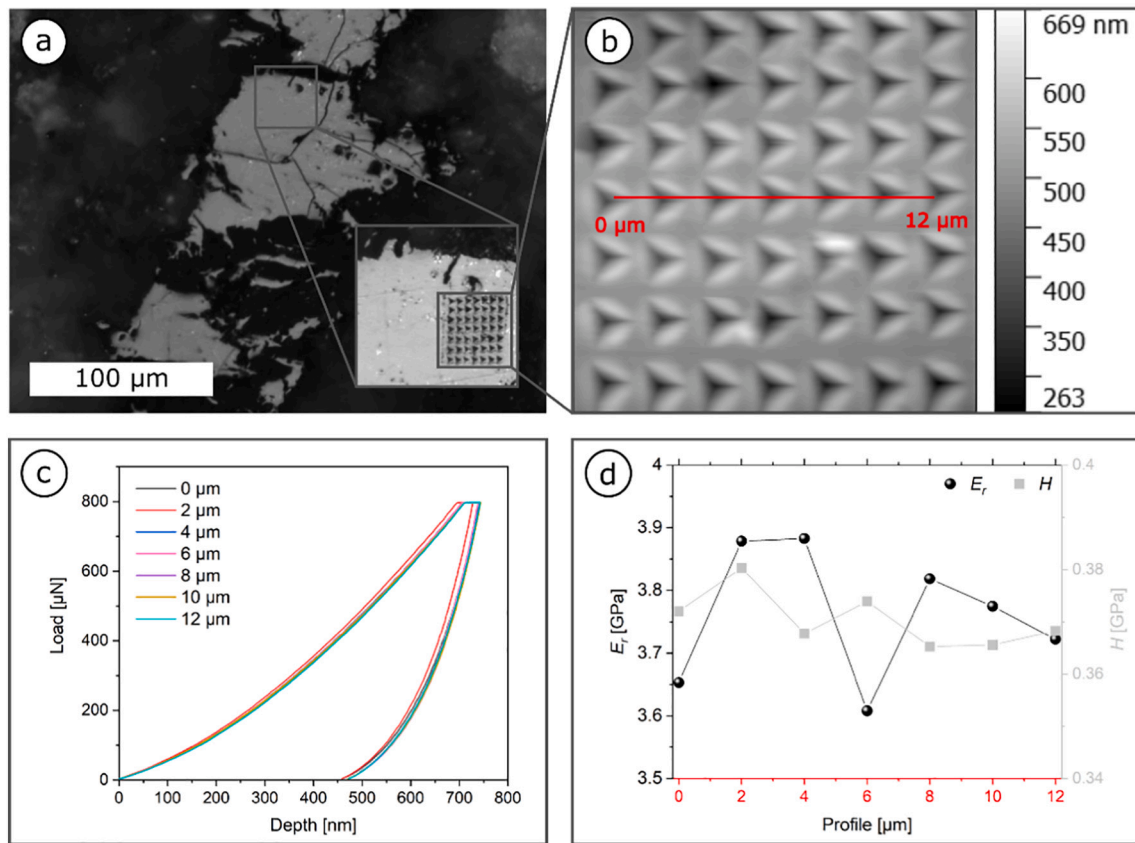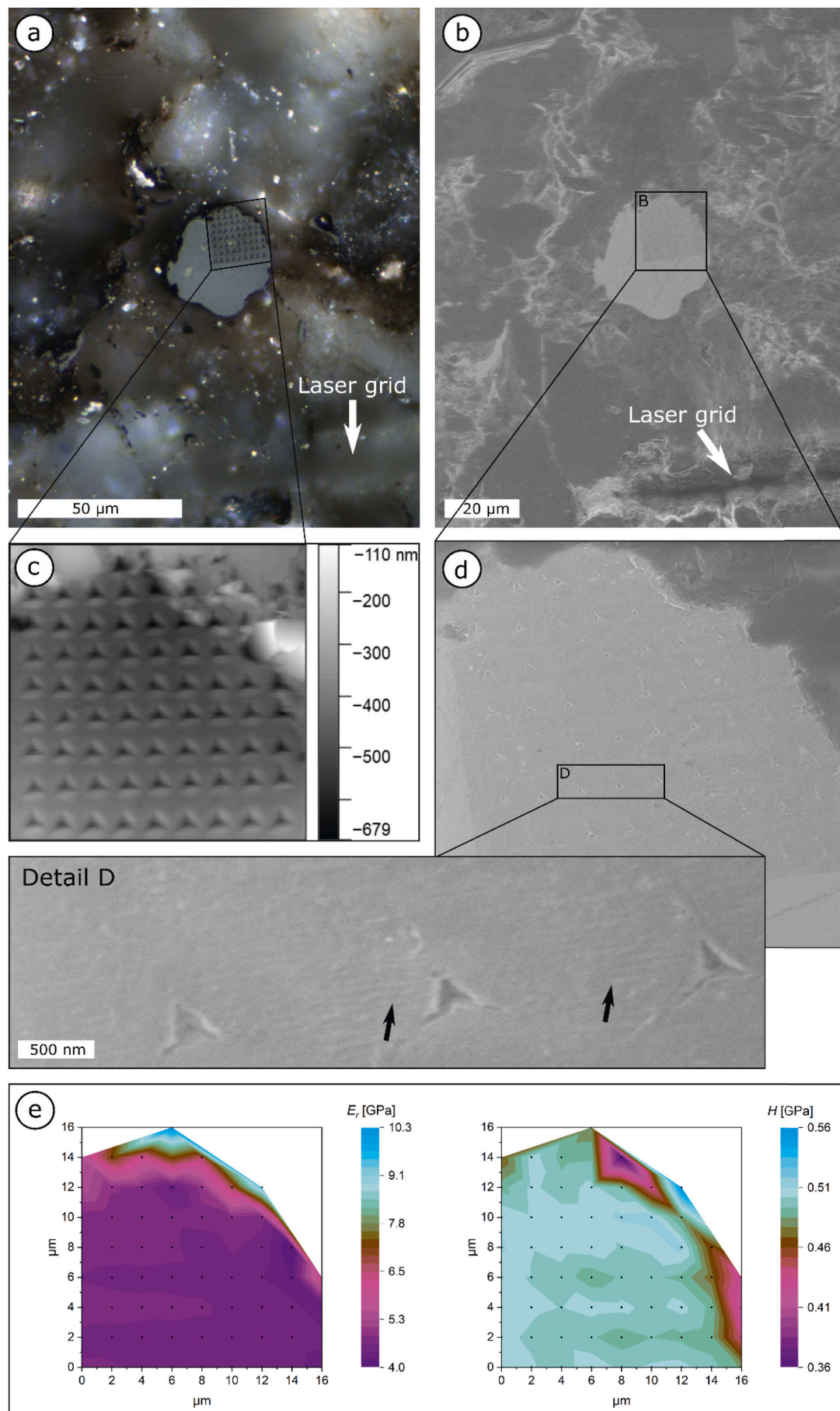
Fig. 10. Optical micrograph of a large vitrinite particle (map 5) in sample SK9 under oil immersion pre and after indention mapping (see inset). (b) SPM surface map (15 × 15 μm) of the tested area and (c) load-displacement curves obtained along the profile (red line in (b)). (d) Slight variations of E_r and H along measured profile (red line in (b)). (For interpretation of the references to color in this figure legend, the reader is referred to the web version of this article.)
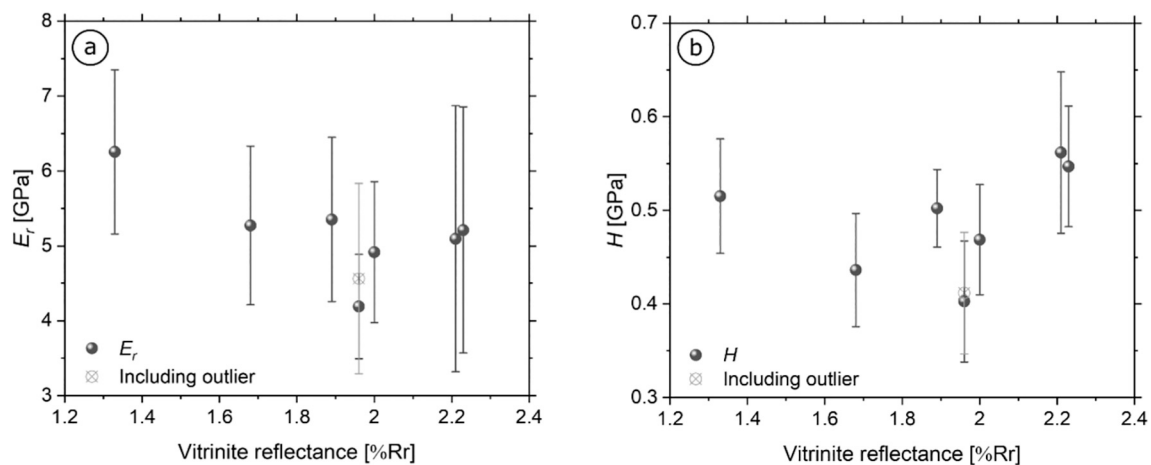
Fig. 11. Averages for (a) E_r and (b) H versus vitrinite reflectance (see Table 3).

this stage. Nevertheless, different character of solid bitumen due to changing organofacies was reported, and particularly the solid bitumen-hosted porosity trends may deviate substantially for changing primary OM composition (Misch et al., 2019a, 2019b), which may result in changing mechanical behavior as well. On the other hand, it may be difficult to delineate between solid bitumen and vitrinite, in cases where soluble bitumen is retained by vitrinite an both form an entity even in overmature state (Cardott et al., 2015; Misch et al., 2019a).

The representative *k*-means central value obtained for E_r of an inertinite particle in sample SK37 (Table A in supplemental, map 1 in

SK37) shows no significant deviation from the values determined for vitrinite in the same specimen. Inertinite is mainly a product of land plant material charred during paleo-wildfires. As a consequence, it shows considerably higher initial C and O contents, as well as lower initial H contents compared to vitrinite and other primary OM types. It is well accepted that structural changes (devolatilization, aromatization) of inertinite occur comparably early during diagenesis (International Committee for Coal and Organic Petrology (ICCP), 2001; Levine, 1993). Furthermore, Vranjes et al. (2018) clearly showed that the micro-mechanical properties of inertinite macerals in coals from the Ukrainian

(caption on next page)

Fig. 12. (a) Optical micrograph (oil immersion) of a vitrinite particle in sample SK12; the corresponding HIM images in (b, d) show a slight alteration (fine lines indicated by variations in SE contrast) of the mapped surface caused by the diamond tip during (c) SPM scanning (20 × 20 μm scan). (e) Corresponding E_r and H property maps (map 4) of the respective area. The black dots represent the positions of individual indents, while the property maps are created by linear interpolation between these values.
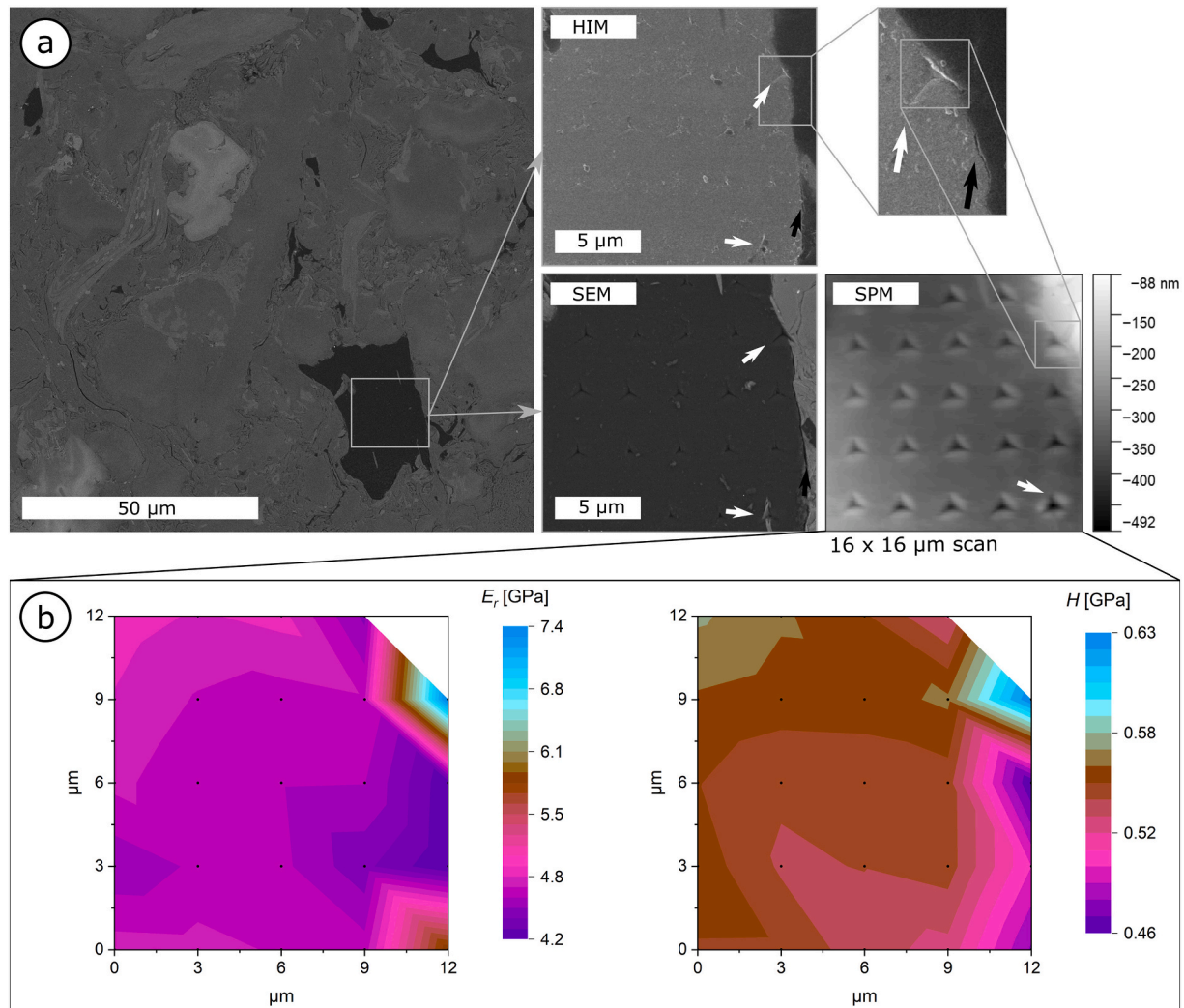
Fig. 13. Correlative analysis of an OM particle (map 5) in sample SK12 including (a) SEM, HIM and SPM (16 × 16 μm scan) imaging (see insets). (b) displays the linearly interpolated E_r and H property maps of the respective area (black dots represent individual indents). Indents in proximity to minerals are indicated by white arrows, while interpreted shrinkage cracks are highlighted by black arrows.

Donets Basin correlate perfectly with the inertinite reflectance, which reflects the temperature conditions during paleo-wildfires and hence pre-depositional processes. In spite of these fundamental differences to the diagenetic evolution of vitrinite, previous studies postulated a converge of properties particularly at high rank >2%Rr (Levine, 1993). Relating this to the overmature state of the samples investigated here, it is reasonable to assume that ongoing homogenization may have occurred, leading to similar material behavior of vitrinite and inertinite.

4.4. Improved workflow and quality control in micromechanical testing

Specimen preparation by a femto-second laser grid (Fig. 1) enabled correlation between imaging and mechanical testing. This approach should be adopted in future micromechanical studies, as a strong interdependency between mechanical parameters and structural features was clearly proven by nanoindentation mapping combined with SEM and HIM (Figs. 12, 13). Material parameters (E_r and H) were

identified from individual OM particles and analyzed by *k*-means clustering. In combination with the SPM images and the correlative high-resolution imaging, the obtained E_r and H clusters were evaluated to identify the reasons behind local variations (e.g., boundary effects, intraparticle heterogeneity, etc.). It proved extremely valuable to be able to trace back to the individual indent in the complementary image data. Thereby, outlier measurements, e.g. due to breakouts along OM – mineral contacts, could easily be identified (Fig. 17). A further enhancement of data quality and property correlations was achieved by the *k*-means++ – enhanced *k*-means clustering of the high-speed nanoindentation mapping data (Figs. 14, 15; Table A in supplemental). Microstructural and thermal maturity influences which were not clearly resolved by the initial data set, became more distinct after cluster-processing (Table 3, Table A in supplemental; Fig. 16). However, further analytical improvements, particularly for the investigation of OM-rich rocks, may be achieved by optimized low- or non-invasive preparation (Hackley et al., 2020; Loucks et al., 2009). Particularly
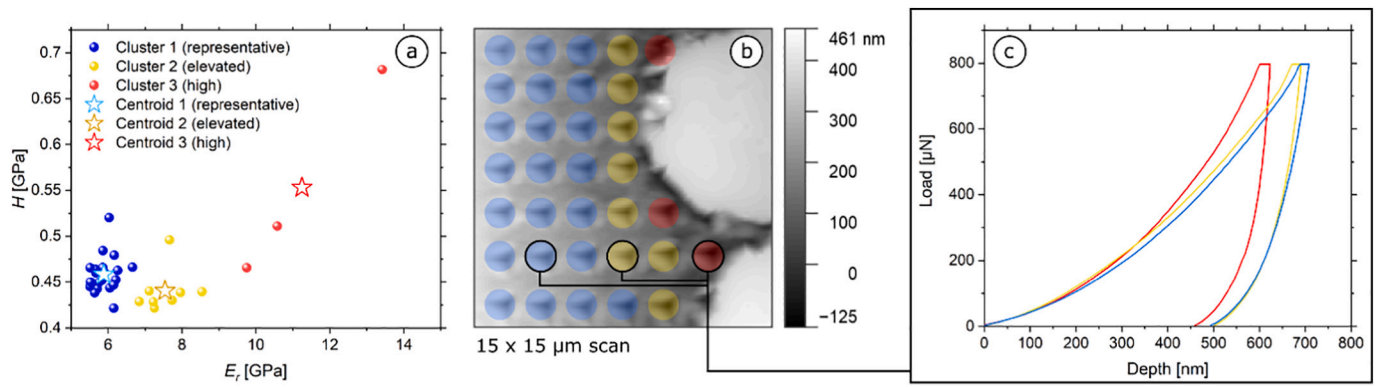
Fig. 14. *k*-means clustering results for a map of sample SK2 (map 1). (a) *H* plotted versus *E*$_r$; the individuall data points are color-coded according to their cluster assignment. The representative centroids are indicated by stars (b) The color-coded nanoindents visualized within an SPM scan. (c) Example of load-displacement curves; the color-coding corresponds to the cluster colors shown in (a) and (b).
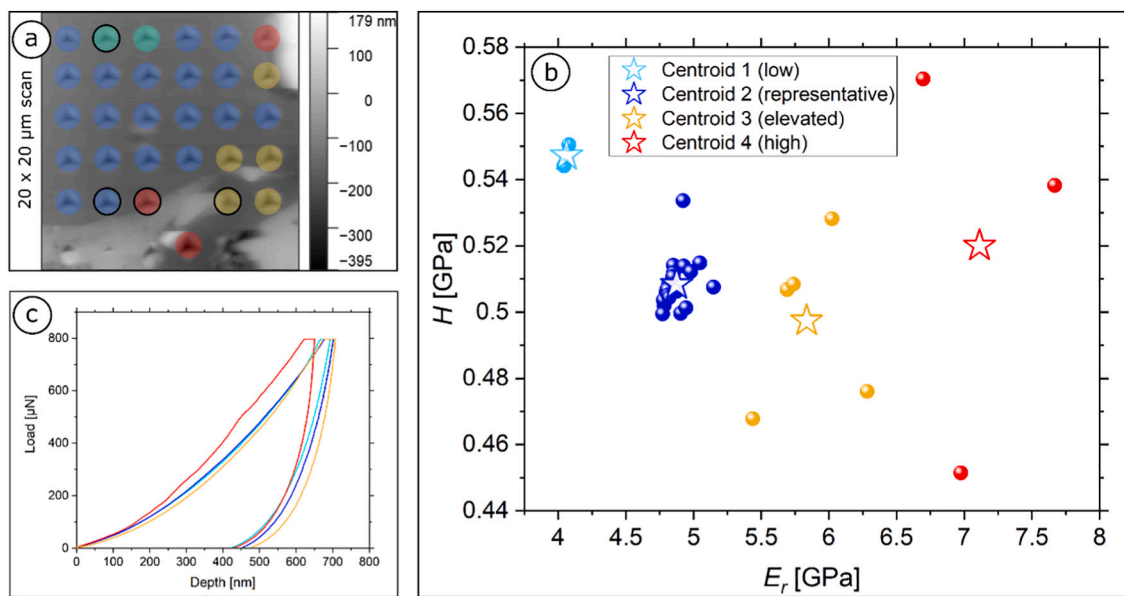

Fig. 15. (a) SPM surface scan of a vitrinite particle in sample SK10 (map 1). The nanoindents are color-coded according to the *k*-means clustering results shown in (b). (c) Load displacement curves for the indents highlighted by black circles in (a).
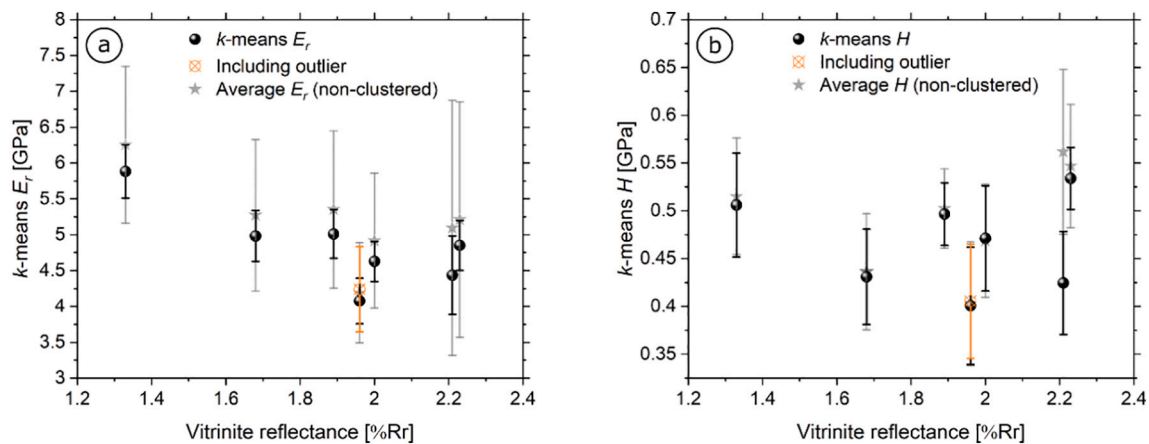

Fig. 16. Average *k*-means representative centroids for (a) *E*$_r$ and (b) *H* plotted against vitrinite reflectance (see Table 5). Non-clustered averages were included for comparison (see Table 4, Fig. 11).

Table 5
Average E_r and H calculated from all data points within the representative clusters for each sample (see Table 4 for average obtained from raw data). (v – vitrinite, sb – solid bitumen, i – inertinite; rep. – representative).

| Name	Depth	VR	Representative average				Indents	OM types	Comments
			k-means E_r	SD	k-means H	SD			
	m	%Rr	GPa	GPa	GPa	GPa	n		
SK2	3376	1.33	5.88	0.37	0.51	0.05	143	v	All data included (rep.)
SK5	3466	1.68	4.98	0.36	0.43	0.05	134	sb	All data included (rep.)
SK9	3586	1.96	4.07	0.32	0.40	0.06	129	v	Outlier excluded (map 1)
			4.24	0.59	0.41	0.06	145	v	All data included (rep.)
SK10	3616	1.89	5.01	0.34	0.50	0.03	160	v	All data included (rep.)
SK12	3676	2.00	4.63	0.28	0.47	0.06	182	v	All data included (rep.)
SK18	3866	2.23	4.85	0.35	0.53	0.03	150	v	All data included (rep.)
			4.81	0.12	0.55	0.01	78	v	Coaly part (maps 1, 2, 3)
			4.90	0.48	0.51	0.03	72	v	Shaly part (maps 4, 5, 6)
SK37	4426	2.21	4.43	0.55	0.42	0.05	122	v, i	All data included (rep.)
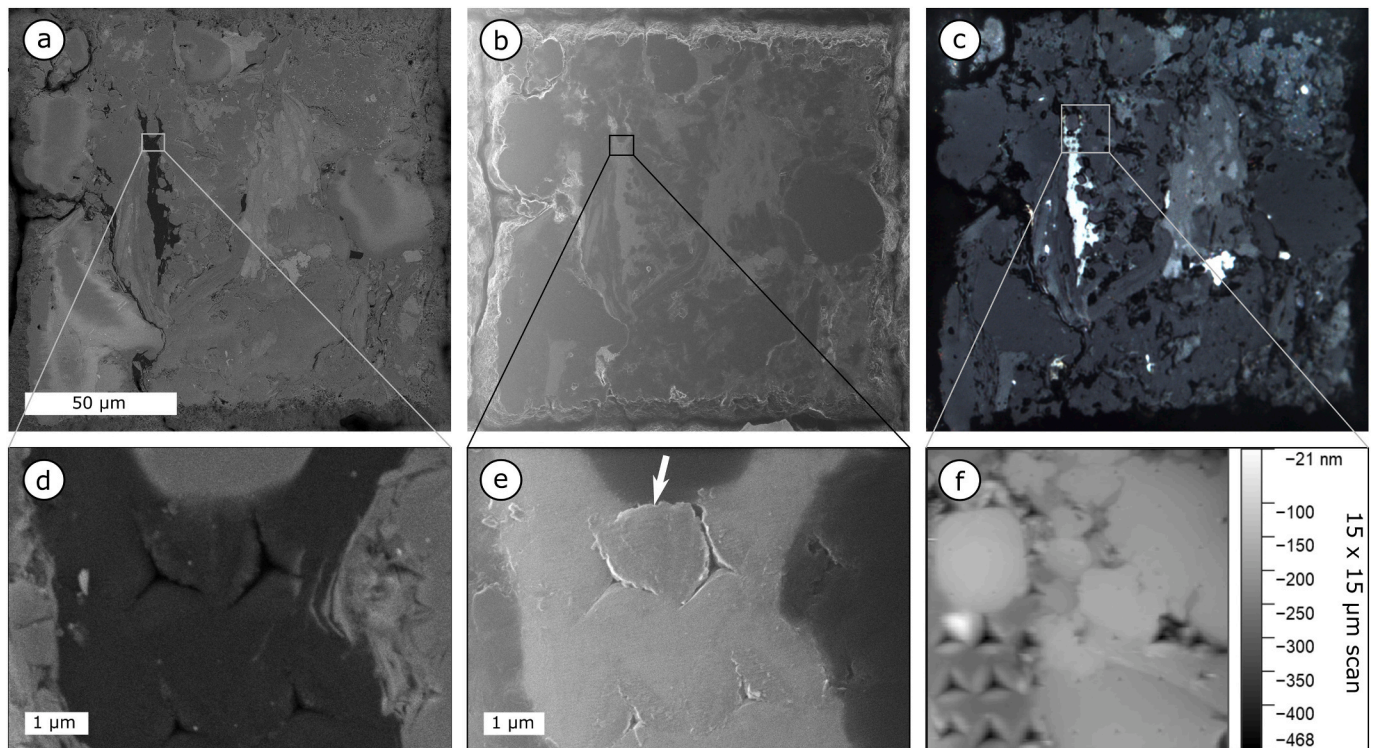
Fig. 17. Correlative imaging of a vitrinite particle within sample SK12 (excluded from quantitative analysis). (a) SEM and (b) HIM and (c) optical (dry state) overview of the laser grid quadrant with detailed excerpts (d, e respectively), (f) SPM image with indicated topographical feature within tested OM area (15 × 15 μm scan). A crack likely resulting from the property mapping can be imaged by means of HIM imaging (see e).

the influence of variations in the array spacing during high-speed property mapping in soft materials such as kerogen and bitumen needs to be addressed further, in order to balance maximum resolution and minimize interference between neighboring indents. Also, the impact of surface alteration by the Cube Corner tip during scanning, which was clearly observed in HIM images (Fig. 12d, detail in D), has to be considered. HIM proved a valuable tool for the detection of such surface effects, as the image contrast created by the helium ion beam is not based on atomic number as compared to an electron beam (Ward et al., 2006), and thus OM structures can be visualized at even higher resolution and topographic sensitivity compared to conventional SEM systems (Bell, 2009; Scipioni et al., 2009). This includes detailed images of indents in OM and at OM/mineral interfaces (Figs. 12, 13), which helped to identify outliers such as nanoindentation-induced cracks at OM – mineral boundaries (Fig. 17).

5. Conclusion

In this study the OM of an over-mature sample set from the Songliao Basin in China was mechanically characterized by a new approach of combined high-speed nanoindentation property mapping, high-resolution imaging and machine learning based data processing. Femto-second laser marked areas enabled a correlative study, which facilitated further evaluation of the mechanically tested areas. In order to gain a better understanding regarding the material characteristics and potential influencing factors, high-resolution SEM and HIM imaging was carried out. The resulting E_r and H data from each high-speed nano-indentation property map was subsequently processed by the unsupervised machine learning algorithm k-means clustering to evaluate the representative material properties of OM particles which in general exhibit inhomogeneous stiffness and thus a large spread of E_r. Enhanced OM modulus values were associated with adjacent mineral matter, while

pores, cracks and surface artifacts likely lead to significantly lowered E_r. The formation of these varying mechanical domains is interpreted to be a result of differential density and compaction of the OM on the sub-micron level. It was also determined that the E_r of OM generally decreases with increasing maturity (from 1.33 to 1.96%Rr), starting with representative average values of 5.88 ± 0.37 down to 4.07 ± 0.32 GPa, while a slight increase is observed between 2.00 and 2.23%Rr (Table 5; Fig. 16a). The respective H averages (ranging between 0.4 and 0.5 GPa) do not exhibit an obvious relation to maturity (Table 5; Fig. 16b). The trend for E_r must be viewed with caution, as the compaction and stress support of the OM particles are likely dependent on the mineral fabric. At comparable maturity, OM within predominant clay matrix (SK10, SK12) exhibits higher E_r results compared to OM embedded within a rock fabric with coarse character (SK9), as the presence of clay minerals favors a more effective compaction (Table 5; see detailed table regarding clustered data in the supplemental material, Table A).

The lacking porosity of kerogen presumably related to pore occlusion by secondary generated bitumen. Although solid bitumen is believed to have similar properties to vitrinite in the over-mature state, it is not yet clear how it affects the mechanical properties of kerogen while occluding pores and forming an interphase. Also, effects on the mechanical characterization such as surface alteration by SPM scanning, general surface roughness and the chosen preparation technique (mechanical vs. ion polishing), as well as indentation spacing, must be taken into consideration.

In conclusion, this approach proved itself extremely valuable for the detailed material characterization of complex and highly inhomogeneous materials. While this already opens a wealth of exciting new possibilities, future studies on this subject shall also focus on the further optimization of the experimental settings and enhancement of the workflow.

Supplementary data to this article can be found online at https://doi.org/10.1016/j.coal.2021.103847.

Declaration of Competing Interest

The authors declare that they have no known competing financial interests or personal relationships that could have appeared to influence the work reported in this paper.

Acknowledgments

References

Abedi, S., Slim, M., Ulm, F.-J., 2016. Nanomechanics of organic-rich shales: the role of thermal maturity and organic matter content on texture. Acta Geotech. 11, 775–787. https://doi.org/10.1007/s11440-016-0476-2.

Ahmadov, R., Vanorio, T., Mavko, G., 2009. Confocal laser scanning and atomic-force microscopy in estimation of elastic properties of the organic-rich Bazhenov Formation. Lead. Edge 28, 18–23. https://doi.org/10.1190/1.3064141.

Alstadt, K.N., Katti, K.S., Katti, D.R., 2016. Nanoscale morphology of kerogen and in situ nanomechanical properties of green river oil shale. J. Nanomech. Micromech. 6, 04015003 https://doi.org/10.1061/(ASCE)NM.2153-5477.0000103.

Arthur, D., Vassilvitskii, S., 2007. K-Means++: The Advantages of Careful Seeding. In: Proc. Eighteenth Annu. ACM-SIAM Symp. Discrete Algorithms, pp. 1027–1035.

Bell, D.C., 2009. Contrast mechanisms and image formation in helium ion microscopy. Microsc. Microanal. 15, 147–153. https://doi.org/10.1017/S1431927609090118.

Bennett, K.C., Berla, L.A., Nix, W.D., Borja, R.I., 2015. Instrumented nanoindentation and 3D mechanistic modeling of a shale at multiple scales. Acta Geotech. 10, 1–14. https://doi.org/10.1007/s11440-014-0363-7.

Bobko, C., Ulm, F.-J., 2008. The nano-mechanical morphology of shale. Mech. Mater. 40, 318–337. https://doi.org/10.1016/j.mechmat.2007.09.006.

Cardott, B.J., Landis, C.R., Curtis, M.E., 2015. Post-oil solid bitumen network in the Woodford Shale, USA — A potential primary migration pathway. Int. J. Coal Geol. 139, 106–113. https://doi.org/10.1016/j.coal.2014.08.012.

Cavanaugh, T., Walls, J., 2016. Multiresolution imaging of shales using electron and helium ion microscopy. In: Olson, T. (Ed.), Imaging Unconventional Reservoir Pore Systems. American Association of Petroleum Geologists, pp. 65–76. https://doi.org/10.1306/13592017M1123693.

Charlet, L., Alt-Epping, P., Wersin, P., Gilbert, B., 2017. Diffusive transport and reaction in clay rocks: a storage (nuclear waste, CO2, H2), energy (shale gas) and water quality issue. Adv. Water Resour. 106, 39–59. https://doi.org/10.1016/j.advwatres.2017.03.019.

Constantinides, G., Ravi Chandran, K.S., Ulm, F.-J., Van Vliet, K.J., 2006. Grid indentation analysis of composite microstructure and mechanics: principles and validation. Mater. Sci. Eng. A 430, 189–202. https://doi.org/10.1016/j.msea.2006.05.125.

Craddock, P.R., Le Doan, T.V., Bake, K., Polyakov, M., Charsky, A.M., Pomerantz, A.E., 2015. Evolution of kerogen and bitumen during thermal maturation via semi-open pyrolysis investigated by infrared spectroscopy. Energy Fuel 29, 2197–2210. https://doi.org/10.1021/ef5027532.

Curtis, M.E., Cardott, B.J., Sondergeld, C.H., Rai, C.S., 2012. Development of organic porosity in the Woodford Shale with increasing thermal maturity. Int. J. Coal Geol. 103, 26–31. https://doi.org/10.1016/j.coal.2012.08.004.

Desheng, L., Renqi, J., Katz, B.J., 1995. Petroleum generation in the nonmarine Qingshankou Formation (Lower Cretaceous), Songliao Basin, China. In: Katz, B.J. (Ed.), Petroleum Source Rocks, Casebooks in Earth Sciences. Springer, Berlin Heidelberg, Berlin, Heidelberg, pp. 131–148. https://doi.org/10.1007/978-3-642-78911-3_8.

Ebenstein, D.M., Pruitt, L.A., 2006. Nanoindentation of biological materials. Nano Today 1, 26–33. https://doi.org/10.1016/S1748-0132(06)70077-9.

Eliyahu, M., Emmanuel, S., Day-Stirrat, R.J., Macaulay, C.I., 2015. Mechanical properties of organic matter in shales mapped at the nanometer scale. Mar. Pet. Geol. 59, 294–304. https://doi.org/10.1016/j.marpetgeo.2014.09.007.

Emmanuel, S., Eliyahu, M., Day-Stirrat, R.J., Hofmann, R., Macaulay, C.I., 2016. Impact of thermal maturation on nano-scale elastic properties of organic matter in shales. Mar. Pet. Geol. 70, 175–184. https://doi.org/10.1016/j.marpetgeo.2015.12.001.

Goldsby, D.L., Rar, A., Pharr, G.M., Tullis, T.E., 2004. Nanoindentation creep of quartz, with implications for rate- and state-variable friction laws relevant to earthquake mechanics. J. Mater. Res. 19, 357–365. https://doi.org/10.1557/jmr.2004.19.1.357.

Hackley, P.C., Lewan, M., 2018. Understanding and distinguishing reflectance measurements of solid bitumen and vitrinite using hydrous pyrolysis: Implications to petroleum assessment. AAPG Bull. 102, 1119–1140. https://doi.org/10.1306/08291717097.

Hackley, P.C., Valentine, B.J., Voortman, L.M., Van Oosten Slingeland, D.S.B., Hatcherian, J., 2017. Utilization of integrated correlative light and electron microscopy (iCLEM) for imaging sedimentary organic matter: utilization of integrated correlative light and electron microscopy. J. Microsc. 267, 371–383. https://doi.org/10.1111/jmi.12576.

Hackley, P.C., Jubb, A.M., Valentine, B.J., Hatcherian, J.J., Yu, J.-J., Podrazky, W.K., 2020. Investigating the effects of broad ion beam milling to sedimentary organic matter: Surface flattening or heat-induced aromatization and condensation? Fuel 282, 118627. https://doi.org/10.1016/j.fuel.2020.118627.

Hackley, P.C., Jubb, A.M., McAleer, R.J., Valentine, B.J., Birdwell, J.E., 2021. A review of spatially resolved techniques and applications of organic petrography in shale petroleum systems. Int. J. Coal Geol. 103745. https://doi.org/10.1016/j.coal.2021.103745.

Hartigan, J.A., Wong, M.A., 1979. Algorithm AS 136: a K-means clustering algorithm. Appl. Stat. 28, 100. https://doi.org/10.2307/2346830.

Hay, J., 2009. Introduction to instrumented indentation testing. Exp. Tech. 33, 66–72. https://doi.org/10.1111/j.1747-1567.2009.00541.x.

Hlawacek, G., Veligura, V., van Gastel, R., Poelsema, B., 2014. Helium ion microscopy. J. Vac. Sci. Technol. B Nanotechnol. Microelectron. Mater. Process. Meas. Phenom. 32, 020801 https://doi.org/10.1116/1.4863676.

Hou, H., Wang, C., Zhang, J., Ma, F., Fu, W., Wang, P., Huang, Y., Zou, C., Gao, Y.f., Gao, Y., Zhang, L., Yang, J., Guo, R., 2018. Deep Continental Scientific Drilling Engineering Project in Songliao Basin: progress in Earth Science research. China Geol. 1, 173–186. https://doi.org/10.31035/cg2018036.

Huang, C., Ju, Y., Zhu, H., Lash, G.G., Qi, Y., Yu, K., Feng, H., Ju, L., Qiao, P., 2020. Investigation of formation and evolution of organic matter pores in marine shale by helium ion microscope: an example from the Lower Silurian Longmaxi Shale, South China. Mar. Pet. Geol. 120, 104550. https://doi.org/10.1016/j.marpetgeo.2020.104550.

Hubbert, M., Rubey, W.W., 1959. Role of fluid pressure in mechanics of overthrust faulting. Geol. Soc. Am. Bull. 70, 115. https://doi.org/10.1130/0016-7606(1959)70[115:ROFPIM]2.0.CO;2.

International Committee for Coal and Organic Petrology (ICCP), 2001. The new inertinite classification (ICCP System 1994). Fuel 80, 459–471. https://doi.org/10.1016/S0016-2361(00)00102-2.

Jakob, S., Pfeifenberger, M.J., Hohenwarter, A., Pippan, R., 2017. Femtosecond laser machining for characterization of local mechanical properties of biomaterials: a case study on wood. Sci. Technol. Adv. Mater. 18, 574–583. https://doi.org/10.1080/14686996.2017.1360751.

Kashinath, A., Szulczewski, M., Dogru, A.H., 2020. Modeling the effect of maturity on the elastic moduli of kerogen using atomistic simulations. Energy Fuel 34, 1378–1385. https://doi.org/10.1021/acs.energyfuels.9b03221.

Khatibi, S., Aghajanpour, A., Ostadhassan, M., Ghanbari, E., Amirian, E., Mohammed, R., 2018. Evaluating the impact of mechanical properties of kerogen on hydraulic fracturing of organic rich formations. In: SPE Canada Unconventional Resources Conference. Presented at the SPE Canada Unconventional Resources Conference, Society of Petroleum Engineers, Calgary, Alberta, Canada. https://doi.org/10.2118/189799-MS.

King, H.E., Eberle, A.P.R., Walters, C.C., Kliewer, C.E., Ertas, D., Huynh, C., 2015. Pore architecture and connectivity in gas shale. Energy Fuel 29, 1375–1390. https://doi.org/10.1021/ef502402e.

Konstantopoulos, G., Koumoulos, E.P., Charitidis, C.A., 2020. Classification of mechanism of reinforcement in the fiber-matrix interface: application of Machine Learning on nanoindentation data. Mater. Des. 192, 108705. https://doi.org/10.1016/j.matdes.2020.108705.

Koumoulos, E.P., Paraskevoudis, K., Charitidis, C.A., 2019. Constituents phase reconstruction through applied machine learning in nanoindentation mapping data of mortar surface. J. Compos. Sci. 3, 63. https://doi.org/10.3390/jcs3030063.

Kranjc, K., Rouse, Z., Flores, K.M., Skemer, P., 2016. Low-temperature plastic rheology of olivine determined by nanoindentation. Geophys. Res. Lett. 43, 176–184. https://doi.org/10.1002/2015GL065837.

Kumar, V., Curtis, M.E., Gupta, N., Sondergeld, C.H., Rai, C.S., 2012a. Estimation of elastic properties of organic matter in woodford shale through nanoindentation measurements. In: SPE Canadian Unconventional Resources Conference. Presented at the SPE Canadian Unconventional Resources Conference, Society of Petroleum Engineers, Calgary, Alberta, Canada. https://doi.org/10.2118/162778-MS.

Kumar, V., Sondergeld, C.H., Rai, C.S., 2012b. Nano to macro mechanical characterization of shale. In: SPE Annual Technical Conference and Exhibition. Presented at the SPE Annual Technical Conference and Exhibition, Society of Petroleum Engineers, San Antonio, Texas, USA. https://doi.org/10.2118/159804-MS.

Kumar, V., Sondergeld, C., Rai, C.S., 2015. Effect of mineralogy and organic matter on mechanical properties of shale. Interpretation 3, SV9–SV15. https://doi.org/10.1190/INT-2014-0238.1.

Landis, C.R., Castaño, J.R., 1995. Maturation and bulk chemical properties of a suite of solid hydrocarbons. Org. Geochem. 22, 137–149. https://doi.org/10.1016/0146-6380(95)90013-6.

Levine, J.R., 1993. Coalification: The Evolution of Coal as Source Rock and Reservoir Rock for Oil and Gas. https://doi.org/10.1306/St38577C3.

Liu, K., Ostadhassan, M., Bubach, B., 2016. Applications of nano-indentation methods to estimate nanoscale mechanical properties of shale reservoir rocks. J. Nat. Gas Sci. Eng. 35, 1310–1319. https://doi.org/10.1016/j.jngse.2016.09.068.

Liu, K., Ostadhassan, M., Bubach, B., Ling, K., Tokhmechi, B., Robert, D., 2018. Statistical grid nanoindentation analysis to estimate macro-mechanical properties of the Bakken Shale. J. Nat. Gas Sci. Eng. 53, 181–190. https://doi.org/10.1016/j.jngse.2018.03.005.

Löhr, S.C., Baruch, E.T., Hall, P.A., Kennedy, M.J., 2015. Is organic pore development in gas shales influenced by the primary porosity and structure of thermally immature organic matter? Org. Geochem. 87, 119–132. https://doi.org/10.1016/j.orggeochem.2015.07.010.

Loucks, R.G., Reed, R.M., Ruppel, S.C., Jarvie, D.M., 2009. Morphology, genesis, and distribution of nanometer-scale pores in siliceous mudstones of the Mississippian Barnett Shale. J. Sediment. Res. 79, 848–861. https://doi.org/10.2110/jsr.2009.092.

Luo, S., Lu, Y., Wu, Y., Song, J., DeGroot, D.J., Jin, Y., Zhang, G., 2020. Cross-scale characterization of the elasticity of shales: statistical nanoindentation and data analytics. J. Mech. Phys. Solids 140, 103945. https://doi.org/10.1016/j.jmps.2020.103945.

Ma, Z., Pathegama Gamage, R., Zhang, C., 2020. Application of nanoindentation technology in rocks: a review. Geomech. Geophys. Geo-Energy Geo-Resour. 6, 60. https://doi.org/10.1007/s40948-020-00178-6.

Mashhadian, M., Verde, A., Sharma, P., Abedi, S., 2018. Assessing mechanical properties of organic matter in shales: results from coupled nanoindentation/SEM-EDX and micromechanical modeling. J. Pet. Sci. Eng. 165, 313–324. https://doi.org/10.1016/j.petrol.2018.02.039.

Mastalerz, M., Drobniak, A., Stankiewicz, A.B., 2018. Origin, properties, and implications of solid bitumen in source-rock reservoirs: a review. Int. J. Coal Geol. 195, 14–36. https://doi.org/10.1016/j.coal.2018.05.013.

Mathia, E.J., Bowen, L., Thomas, K.M., Aplin, A.C., 2016. Evolution of porosity and pore types in organic-rich, calcareous, Lower Toarcian Posidonia Shale. Mar. Pet. Geol. 75, 117–139. https://doi.org/10.1016/j.marpetgeo.2016.04.009.

Milliken, K.L., Rudnicki, M., Awwiller, D.N., Zhang, T., 2013. Organic matter-hosted pore system, Marcellus Formation (Devonian), Pennsylvania. AAPG Bull. 97, 177–200. https://doi.org/10.1306/07231212048.

Misch, D., Klaver, J., Gross, D., Mayer-Kiener, V., Mendez-Martin, F., Schmatz, J., Sachsenhofer, R.F., 2018. Factors controlling shale microstructure and porosity: a case study on upper Visean Rudov beds from the Ukrainian Dneiper–Donets Basin. AAPG Bull. 102, 2629–2654. https://doi.org/10.1306/05111817295.

Misch, D., Gross, D., Hawranek, G., Horsfield, B., Klaver, J., Mendez-Martin, F., Urai, J.L., Vranjes-Wessely, S., Sachsenhofer, R.F., Schmatz, J., Li, J., Zou, C., 2019a. Solid bitumen in shales: petrographic characteristics and implications for reservoir characterization. Int. J. Coal Geol. 205, 14–31. https://doi.org/10.1016/j.coal.2019.02.012.

Misch, D., Riedl, F., Liu, B., Horsfield, B., Ziegs, V., Mendez-Martin, F., Vranjes-Wessely, S., Sachsenhofer, R.F., 2019b. Petrographic and sorption-based characterization of bituminous organic matter in the Mandal Formation, Central Graben (Norway). Int. J. Coal Geol. 211, 103229. https://doi.org/10.1016/j.coal.2019.103229.

Misch, D., Klaver, J., Gross, D., Rustamov, J., Sachsenhofer, R.F., Schmatz, J., Urai, J.L., 2020. Pore space characteristics of the Upper Visean 'Rudov Beds': insights from broad ion beam scanning electron microscopy and organic geochemical investigations. Geol. Soc. Lond. Spec. Publ. 484, 205–228. https://doi.org/10.1144/SP484.9.

Nečas, D., Klapetek, P., 2012. Gwyddion: an open-source software for SPM data analysis. Open Phys. 10 https://doi.org/10.2478/s11534-011-0096-2.

Noah, M., Horsfield, B., Han, S., Wang, C., 2020. Precise maturity assessment over a broad dynamic range using polycyclic and heterocyclic aromatic compounds. Org. Geochem. 148, 104099. https://doi.org/10.1016/j.orggeochem.2020.104099.

Oliver, W.C., Pharr, G.M., 1992. An improved technique for determining hardness and elastic modulus using load and displacement sensing indentation experiments. J. Mater. Res. 7, 1564–1583. https://doi.org/10.1557/JMR.1992.1564.

Oliver, W.C., Pharr, G.M., 2004. Measurement of hardness and elastic modulus by instrumented indentation: advances in understanding and refinements to methodology. J. Mater. Res. 19, 3–20. https://doi.org/10.1557/jmr.2004.19.1.3.

Oliver, W.C., Pharr, G.M., 2010. Nanoindentation in materials research: past, present, and future. MRS Bull. 35, 897–907. https://doi.org/10.1557/mrs2010.717.

Oyen, M.L., 2013. Nanoindentation of biological and biomimetic materials. Exp. Tech. 37, 73–87. https://doi.org/10.1111/j.1747-1567.2011.00716.x.

Pedregosa, F., Varoquaux, G., Gramfort, A., Michel, V., Thirion, B., Grisel, O., Blondel, M., Prettenhofer, P., Weiss, R., Dubourg, V., Vanderplas, J., Passos, A., Cournapeau, D., Brucher, M., Perrot, M., Duchesnay, É., 2011. Scikit-learn: machine learning in Python. J. Mach. Learn. Res. 12, 2825–2830.

Peng, S., Yang, J., Xiao, X., Loucks, B., Ruppel, S.C., Zhang, T., 2015. An integrated method for upscaling pore-network characterization and permeability estimation: example from the Mississippian Barnett Shale. Transp. Porous Media 109, 359–376. https://doi.org/10.1007/s11242-015-0523-8.

Pfeifenberger, M.J., Mangang, M., Wurster, S., Reiser, J., Hohenwarter, A., Pfleging, W., Kiener, D., Pippan, R., 2017. The use of femtosecond laser ablation as a novel tool for rapid micro-mechanical sample preparation. Mater. Des. 121, 109–118. https://doi.org/10.1016/j.matdes.2017.02.012.

Pfeifenberger, M.J., Milassin, G., Hohenwarter, A., Putz, B., Semprimoschnig, C.O.A., Pippan, R., 2019. Electron irradiation effects on strength and ductility of polymer foils studied by femtosecond laser-processed micro-tensile specimens. Materials 12, 1468. https://doi.org/10.3390/ma12091468.

Revil, A., Grauls, D., Brévart, O., 2002. Mechanical compaction of sand/clay mixtures: compaction of sand-clay mixtures. J. Geophys. Res. Solid Earth 107, ECV 11-1–ECV 11-15. https://doi.org/10.1029/2001JB000318.

Rousseeuw, P.J., 1987. Silhouettes: a graphical aid to the interpretation and validation of cluster analysis. J. Comput. Appl. Math. 20, 53–65. https://doi.org/10.1016/0377-0427(87)90125-7.

Sayers, C.M., 2013. The effect of kerogen on the elastic anisotropy of organic-rich shales. Geophysics 78, D65–D74. https://doi.org/10.1190/geo2012-0309.1.

Schieber, J., 2013. SEM observations on ion-milled samples of Devonian Black shales from Indiana and New York. The petrographic context of multiple pore types. In: Electron Microscopy of Shale Hydrocarbon Reservoirs. American Association of Petroleum Geologists. https://doi.org/10.1306/13391711M1023589.

Scipioni, L., Sanford, C.A., Notte, J., Thompson, B., McVey, S., 2009. Understanding imaging modes in the helium ion microscope. J. Vac. Sci. Technol. B Microelectron. Nanometer Struct. 27, 3250. https://doi.org/10.1116/1.3258634.

Shukla, P., Kumar, V., Curtis, M., Sondergeld, C.H., Rai, C.S., 2013. Nanoindentation studies on shales. In: ARMA 13-578, 47th U.S. Rock Mechanics/Geomechanics Symposium, San Francisco, California.

Shukla, P., Taneja, S., Sondergeld, C., Rai, C., 2015. Nanoindentation Measurements on Rocks. In: Carroll, J., Daly, S. (Eds.), Fracture, Fatigue, Failure, and Damage Evolution, Conference Proceedings of the Society for Experimental Mechanics Series, vol. 5. Springer International Publishing, Cham, pp. 99–105. https://doi.org/10.1007/978-3-319-06977-7_13.

Sijbrandij, S., Notte, J., Sanford, C., Hill, R., 2010. Analysis of subsurface beam spread and its impact on the image resolution of the helium ion microscope. J. Vac. Sci. Technol. B Nanotechnol. Microelectron. Mater. Process. Meas. Phenom. 28, C6F6–C6F9. https://doi.org/10.1116/1.3497012.

Sudharshan Phani, P., Oliver, W.C., 2019. A critical assessment of the effect of indentation spacing on the measurement of hardness and modulus using instrumented indentation testing. Mater. Des. 164, 107563. https://doi.org/10.1016/j.matdes.2018.107563.

Thom, C., Goldsby, D., 2019. Nanoindentation studies of plasticity and dislocation creep in halite. Geosciences 9, 79. https://doi.org/10.3390/geosciences9020079.

Thorndike, R.L., 1953. Who belongs in the family? Psychometrika 18, 267–276. https://doi.org/10.1007/BF02289263.

Ulm, F.-J., Abousleiman, Y., 2006. The nanogranular nature of shale. Acta Geotech. 1, 77–88. https://doi.org/10.1007/s11440-006-0009-5.

Valenza, J.J., Drenzek, N., Marques, F., Pagels, M., Mastalerz, M., 2013. Geochemical controls on shale microstructure. Geology 41, 611–614. https://doi.org/10.1130/G33639.1.

Vignesh, B., Oliver, W.C., Kumar, G.S., Phani, P.S., 2019. Critical assessment of high speed nanoindentation mapping technique and data deconvolution on thermal barrier coatings. Mater. Des. 181, 108084. https://doi.org/10.1016/j.matdes.2019.108084.

Vranjes, S., Misch, D., Schöberl, T., Kiener, D., Gross, D., Sachsenhofer, R.F., 2018. Nanoindentation study of macerals in coals from the Ukrainian Donets Basin. Adv. Geosci. 45, 73–83. https://doi.org/10.5194/adgeo-45-73-2018.

Vranjes-Wessely, S., Misch, D., Issa, I., Kiener, D., Fink, R., Seemann, T., Liu, B., Rantitsch, G., Sachsenhofer, R.F., 2020. Nanoscale pore structure of Carboniferous

coals from the Ukrainian Donets Basin: a combined HRTEM and gas sorption study. Int. J. Coal Geol. 224, 103484. https://doi.org/10.1016/j.coal.2020.103484.

Wang, P., Zhang, C., Li, X., Zhang, K., Yuan, Y., Zang, X., Cui, W., Liu, S., Jiang, Z., 2020. Organic matter pores structure and evolution in shales based on the he ion microscopy (HIM): a case study from the Triassic Yanchang, Lower Silurian Longmaxi and Lower Cambrian Niutitang shales in China. J. Nat. Gas Sci. Eng. 84, 103682. https://doi.org/10.1016/j.jngse.2020.103682.

Ward, B.W., Notte, J.A., Economou, N.P., 2006. Helium ion microscope: a new tool for nanoscale microscopy and metrology. J. Vac. Sci. Technol. B Microelectron. Nanometer Struct. 24, 2871. https://doi.org/10.1116/1.2357967.

Wei, L., Mastalerz, M., Schimmelmann, A., Chen, Y., 2014. Influence of Soxhlet-extractable bitumen and oil on porosity in thermally maturing organic-rich shales. Int. J. Coal Geol. 132, 38–50. https://doi.org/10.1016/j.coal.2014.08.003.

Wu, T., Zhao, J., Zhang, W., Zhang, D., 2020. Nanopore structure and nanomechanical properties of organic-rich terrestrial shale: an insight into technical issues for hydrocarbon production. Nano Energy 69, 104426. https://doi.org/10.1016/j.nanoen.2019.104426.

Yang, J., Hatcherian, J., Hackley, P.C., Pomerantz, A.E., 2017. Nanoscale geochemical and geomechanical characterization of organic matter in shale. Nat. Commun. 8, 2179. https://doi.org/10.1038/s41467-017-02254-0.

Yang, C., Xiong, Y., Wang, J., Li, Y., Jiang, W., 2020. Mechanical characterization of shale matrix minerals using phase-positioned nanoindentation and nano-dynamic mechanical analysis. Int. J. Coal Geol. 229, 103571. https://doi.org/10.1016/j.coal.2020.103571.

Yin, H., Zhang, G., 2011. Nanoindentation behavior of muscovite subjected to repeated loading. J. Nanomech. Micromech. 1, 72–83. https://doi.org/10.1061/(ASCE)NM.2153-5477.0000033.

Zargari, S., Wilkinson, T.M., Packard, C.E., Prasad, M., 2016. Effect of thermal maturity on elastic properties of kerogen. Geophysics 81, M1–M6. https://doi.org/10.1190/geo2015-0194.1.

Zeszotarski, J.C., Chromik, R.R., Vinci, R.P., Messmer, M.C., Michels, R., Larsen, J.W., 2004. Imaging and mechanical property measurements of kerogen via nanoindentation. Geochim. Cosmochim. Acta 68, 4113–4119. https://doi.org/10.1016/j.gca.2003.11.031.

Zhao, J., Zhang, W., Zhang, D., Wei, R., Wang, Y., 2020. Influence of geochemical features on the mechanical properties of organic matter in shale. J. Geophys. Res. Solid Earth 125. https://doi.org/10.1029/2020JB019809.

Zhu, W., Hughes, J.J., Bicanic, N., Pearce, C.J., 2007. Nanoindentation mapping of mechanical properties of cement paste and natural rocks. Mater. Charact. 58, 1189–1198. https://doi.org/10.1016/j.matchar.2007.05.018.